communications chemistry

Article

A Nature Portfolio journal

https://doi.org/10.1038/s42004-025-01558-3

A mechanistic model of pure and lipidic α-synuclein aggregation for advancing Parkinson's therapies

Elena Righetti [1,2] ✉, Luca Marchetti [1,2], Enrico Domenici [1,2] & Federico Reali [1] ✉

Alpha-synuclein (aSyn) plays a crucial role in Parkinson's disease, with various aggregates proposed as pathogenic triggers and therapeutic targets. However, anti-aSyn aggregation compounds often fail due to limited knowledge of the underlying molecular basis. In particular, interactions with lipid membranes are central to both physiological and pathological roles of aSyn, yet their underlying mechanisms remain unclear. Disrupting this balance may drive Parkinson's onset and progression, underscoring the need for a mechanistic understanding of pure and lipid-mediated aggregation. Building on well-established in vitro aggregation studies, we propose a mathematical model of aSyn accumulation incorporating both aggregation routes via a nucleation-conversion-polymerization process with self-amplifying loops and toxic oligomers. Model calibration uses data from in vitro assays mimicking physiologically relevant conditions, providing insights into transient and stable aSyn intermediates. Incorporating aSyn-lipid interactions enables in silico exploration of how lipid-to-aSyn ratio influences aggregation, with possible implications for neurodegeneration. Sensitivity analysis highlights secondary nucleation inhibition as a potential anti-aggregation strategy. Overall, our work contributes to a unified framework for investigating in vitro aSyn aggregation and evaluating Parkinson's therapies by building on existing models. It can serve as a stand-alone tool and a modular component in multiscale models, with potential applications in quantitative systems pharmacology.

The neuronal protein alpha-synuclein (aSyn) and its aggregation play a critical role in the onset and progression of Parkinson's disease (PD). This close connection between aSyn and PD pathology is underscored by recent advances in aSyn-based biomarkers, which have defined a new biological framework for the disease[1,2]. Moreover, different aSyn aggregates have been suggested as crucial pathogenic triggers of PD neurodegeneration and considered potential therapeutic targets. Therefore, each new insight into aSyn molecular landscape, and ultimately its thorough understanding, could serve as a linchpin for the rational design of anti-aSyn aggregation therapies.

Over the past few decades, significant progress has been made in characterizing aSyn aggregation. It is well-established that, upon misfolding due to post-translational modifications, increased oxidative stress, or other cellular stressors, aSyn monomers slowly aggregate into oligomeric species, thus creating nucleation seeds. In return, seeding-competent oligomers can rapidly accumulate, forming protofibrils and insoluble fibrils. Multiple aSyn species eventually gather into large cytoplasmic inclusions known as Lewy bodies (LBs) and Lewy neurites (LNs), representing one of PD main molecular hallmarks. The transition from monomers to fibrils through multiple intermediate species relies on a complex molecular network. The resulting aggregates differ in size, conformational structure, and role in the aggregation pathway. The mechanisms involved can be divided into primary and secondary reactions, and their corresponding reverse reactions. Primary events include (i) homogeneous and heterogeneous (i.e., surface-catalyzed) nucleation mechanisms combining monomers into nucleation seeds, i.e., newly formed oligomers, as the first step of the aggregation cascade, (ii) conformational changes between intermediate aggregates, and (iii) fibril formation and elongation by monomer addition. On the other hand, nucleation catalyzed by the surface of existing fibrils and fibril fragmentation are labeled as secondary events, resulting in positive feedback loops.

Uncontrolled accumulation hinges on aSyn oligomers, which have been identified as crucial early steps of the aggregation pathway and suggested as key contributors to PD neurodegeneration. Two oligomeric species, i.e., type-A and type-B oligomers, have been differentiated based on their structural conformation and degradation susceptibility[3,4]. Type-A oligomers are intrinsically disordered and highly susceptible to proteinase-K treatment, whereas type-B oligomers have a partially formed fibrillar

[1]Fondazione The Microsoft Research - University of Trento Centre for Computational and Systems Biology (COSBI), Rovereto, Italy. [2]Department of Cellular, Computational and Integrative Biology (CIBIO), University of Trento, Trento, Italy. ✉e-mail: righetti@cosbi.eu; reali@cosbi.eu

structure characterized by high β-sheet content and high resistance to proteinase-K degradation. This distinction arises not only from the different structural conformations of type-A and type-B oligomers but also from their related roles in the process. Experimental evidence points to oligomers as the major source of inherent toxicity within the aggregation pathway, compared to insoluble aggregates such as mature fibrils and Lewy bodies. Indeed, oligomer formation results in higher levels of oxidative stress, increased cell membrane permeability, deregulated calcium and metal ion homeostasis, impaired mitochondrial function, and dysfunctional protein degradation[5,6]. In this context, type-B oligomers have been suggested as the most cytotoxic aSyn species due to their specific conformation associated with high degrees of β-sheet content and hydrophobic exposure, in contrast to non-toxic type-A oligomers[3,5]. For instance, cell-free in vitro and in vivo experiments have shown that these oligomers can rapidly and significantly increase cytoplasmic reactive oxygen species (ROS) production[3,4,7]. These oligomeric species are sequential intermediates in fibril formation, thus defined as on-pathway. Given the heterogeneous and elusive nature of oligomers, additional species may result from side reactions (i.e., off-pathway), depending on experimental conditions and cellular co-factors, and their presence cannot be ruled out[5,8–10]. However, we focus on type-A and type-B oligomers as they represent the primary path to fibrils in aSyn aggregation[11,12].

Strong evidence also supports co-aggregation between aSyn and lipid molecules, both in vivo and in vitro, in the pathological scenario. For instance, Lewy bodies have been observed as cytoplasmic deposits of aSyn filaments alongside crowded membranes from vesicles and fragmented organelles[13], potentially incorporated at every stage in the formation process[14]. In more controlled environments such as in vitro aggregation assays, lipid-protein co-assemblies can spontaneously form from mixtures of monomeric protein and negatively charged lipid membranes, typically introduced as small unilamellar vesicles (SUVs). Different factors, e.g., vesicle composition and lipid-to-aSyn ratio, affect the co-aggregation process, thus modulating fibril morphology and aggregation kinetics[14]. Galvagnion et al.[15] showed that lipid-aSyn binding can lead to the rapid but reversible breakup of vesicles into small disc-like lipid-protein structures that mediate favorable protein-protein interactions, inducing aggregation. As a result, lipidic fibrils emerge as lipid-aSyn co-aggregates, differing from pure protein fibrils in flexibility and thermodynamical stability. Nonetheless, these species share a connection. Despite these differences, lipid-decorated fibrils can undergo structural conversion upon heating or proteolytic protein removal, potentially transitioning into pure protein fibrils[15]. Pure protein and lipidic fibrils not only differ in structure but also in their modes of formation. Both fibrillar species result from monomer nucleation and oligomeric conversion but differ in the elongation mechanism. Indeed, new mechanistic insights suggest that lipids act as reactants consumed during aggregation, wherein the interaction of existing fibrils with monomer-coated lipid vesicles boosts fibril elongation[15,16].

These insights result from the extensive study of aSyn aggregation in test-tube, in vitro, and in vivo experiments[17,18]. Of particular interest, due to their invaluable contribution to the field, are the chemical kinetic models, developed to complement test-tube experiments. Evolving alongside advancing methodologies for aggregate detection, these models aim to determine the microscopic events that govern aggregation and their kinetic rates under specific experimentally controlled scenarios[16,17,19,20].

Notwithstanding ongoing progress in understanding the central role of aSyn aggregation in PD neurodegeneration, many unclear aspects still hamper the quest for effective disease-modifying therapies, which remain unavailable to date. Indeed, the biological complexity of the aggregation process comes with the limited availability of experimental measurements of aSyn intracellular dynamics, particularly in cell cultures and living systems. This data paucity often results from technical difficulties in tracking aggregate formation over time and addressing the heterogeneous and elusive nature of oligomers. As a result, a quantitative analysis of the aggregation kinetics in these settings requires continuous improvement. Moreover, different aspects of aSyn-lipid interplay are still elusive since this protein interacts with lipid membranes as part of both its physiological and pathological roles in the brain. Its unfolded form has essential functions mainly associated with the synaptic vesicles. The most agreed-upon yet elusive activity involves a lipid-bound helical form regulating synaptic vesicle recycling and neurotransmitter release through interactions with phospholipids of synaptic vesicle membranes[21,22]. On the other hand, aSyn-lipid co-aggregation can have pathological consequences: lipid membranes interfere with aggregation, and, in turn, various aSyn species can lead to alterations in membrane morphology and permeability, resulting in a vicious cycle. A slight perturbation of this finely-tuned balance between functional and deleterious interactions of aSyn and lipids may result in PD pathogenicity[23]. Therefore, understanding the mechanisms underlying aSyn-lipid interactions and the interplay between pure and lipidic aSyn aggregation can lead to crucial physiological implications.

These knowledge gaps would benefit from a unified mechanistic framework for in vitro aSyn aggregation that builds on existing insights to explore new scenarios in silico and support therapeutic development. Such a framework would also strengthen multiscale modeling approaches that connect molecular events to cellular, tissue, and clinical outcomes, particularly in quantitative systems pharmacology (QSP) and physiologically based pharmacokinetic (PBPK) models. While these models account for various biological processes (e.g., degradation pathways and oxidative stress), they often simplify aSyn aggregation, reducing its complexity to coarse-grained variables that overlook the details of aggregation kinetics[24]. Conversely, when aggregation is explicitly modeled, kinetic parameters are often drawn from diverse literature sources[25], which can lead to inconsistencies due to differences in experimental conditions, some of which do not reflect physiological environments. Integrating a unified molecular-level model of aSyn aggregation into these multiscale frameworks would provide a clearer link between microscopic aggregation events and system-level proteostasis failure, leading to a bridge between in vitro findings and in vivo disease mechanisms and deepening our understanding of PD neurodegeneration[26–29].

Results

Chemical kinetic models have provided significant insights into in vitro aSyn aggregation[16,17,19,20]. Tailored to ad-hoc test-tube experiments, they typically include a minimal set of reactions relevant to aggregation, following the principle of model parsimony. By leveraging their framework and mechanistic insights, we developed a mathematical model that integrates pure and lipid-mediated aggregation pathways into a unified framework grounded in in vitro knowledge. This approach allows to explore diverse experimental conditions and aggregation dynamics while aligning with established findings.

Model structure

The system includes microscopic events involved in pure protein and lipidic aggregation and are specifically related to aSyn as reported in the literature. As shown in Fig. 1, it represents a nucleation-conversion-polymerization process that describes fibril formation from monomers via oligomeric intermediates. It explicitly accounts for two oligomeric species and the corresponding monomer-independent conversion steps en route to fibrils, from type-A to type-B oligomers to fibrils. Type-A oligomers appear early in the process, resulting from different primary nucleation mechanisms. They can dissociate back into monomers or undergo a structural conversion that results in type-B oligomers, which eventually form fibrils through another conformational change and do not spontaneously revert to type-A oligomers. Similarly, fibrils do not convert back to type-B oligomers. Structural transitions in amyloid aggregation pathways often result in more stable species and can therefore be effectively treated as irreversible[30]. Accordingly, we consider type-B oligomer formation as a unidirectional process, as these oligomers exhibit increased structural stability and resistance to reversal, making the relatively slow reverse reaction negligible. This assumption aligns with existing chemical kinetic models of aSyn aggregation that explicitly include type-A and type-B oligomers[3,30,31]. Additionally, the system accounts for pure protein and lipidic fibrils[15,16,32], thus reflecting another critical biological and mechanistic distinction between aSyn species.

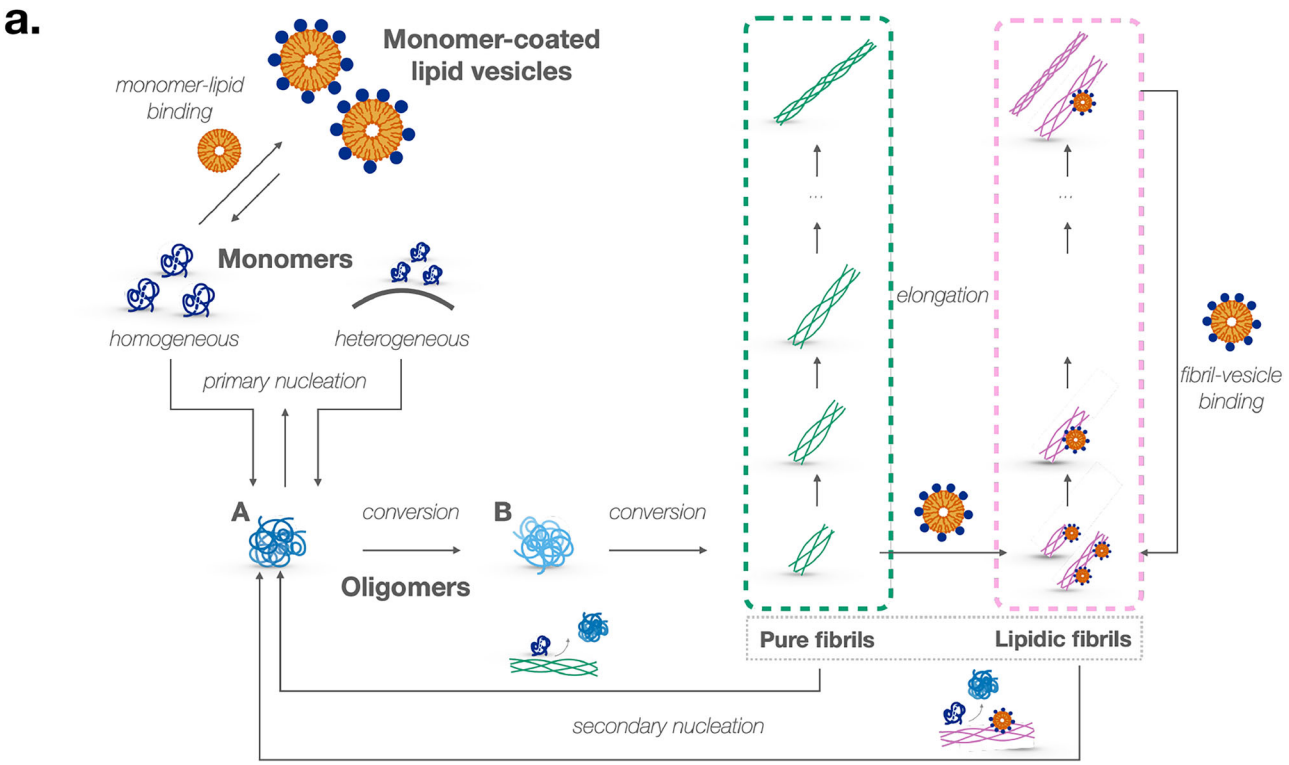

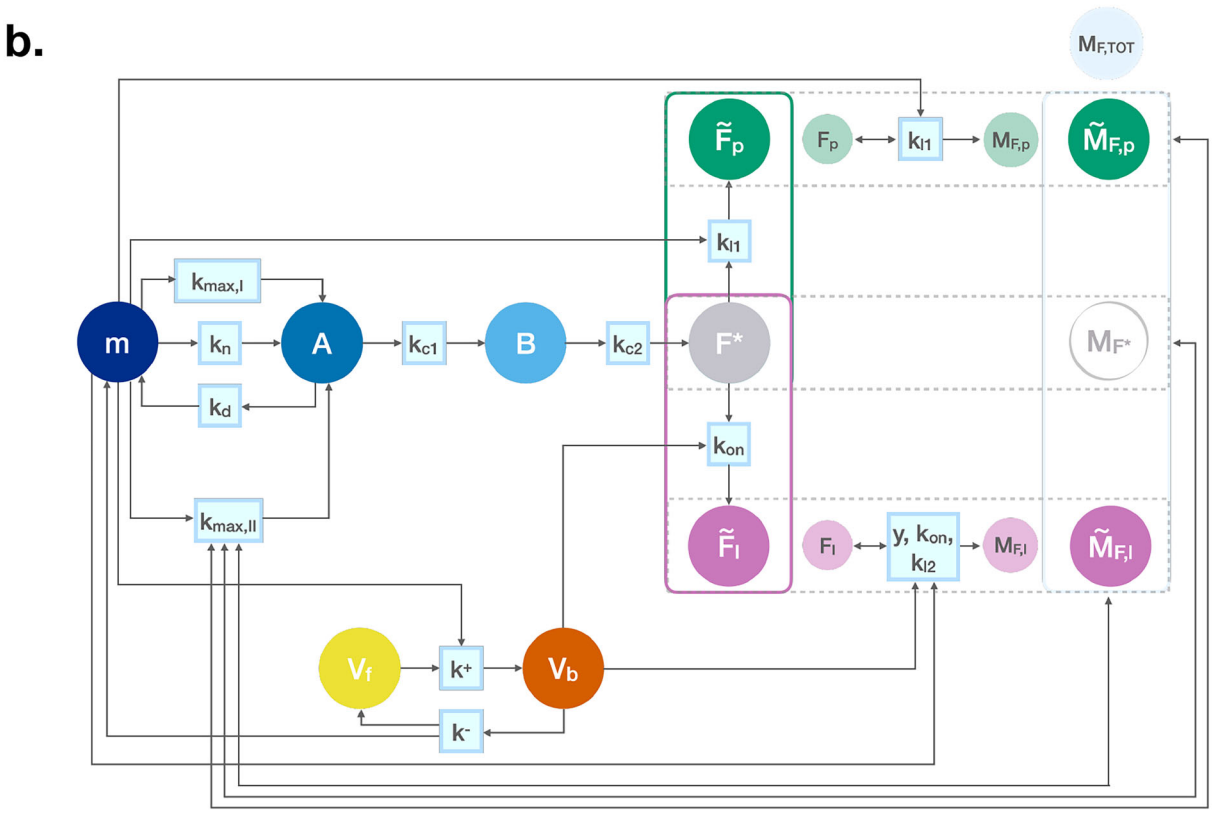

The model describes the temporal evolution of protein species, including free and vesicle-bound monomers (m and m_b), type-A and type-B oligomers (A and B), newly formed fibrils (F^*), pure protein and lipidic fibrils (F_p and F_l), as well as free, monomer-coated, and fibril-bound vesicles (V_f, V_b, and $V_{F,b}$). In addition to monitoring the number concentration of each aSyn species, the model also incorporates mass concentration to keep track of the monomer molecule count within each aSyn species. Such a choice of variable follows the chemical kinetic framework proposed by Knowles and colleagues[17] by leveraging a (stochastic) master equation approach[33], detailed in the Material and

Fig. 1 | Graphical representation of aSyn aggregation. a A conceptual scheme of pure protein and lipidic aggregation pathways represented in our model, including all microscopic events involved in a nucleation-conversion-polymerization process and the interactions between aSyn and lipidic vesicles. Green and pink boxes represent pure protein and lipidic aggregation pathways, respectively. The two oligomeric species are explicitly represented due to their crucial role in aggregation-related cytotoxicity. **b** Model diagram. Circles correspond to the system variables, i.e., monomers (m), type-A and type-B oligomers (A and B), newly generated fibrils (F^*), pure and lipidic fibrils in terms of both number concentration (F_p and F_l) and mass concentration ($M_{F,\mathrm{p}}$ and $M_{F,\mathrm{l}}$), and free and bound vesicles (V_f and V_b); with $\tilde{F}_\mathrm{p}$ and $\tilde{F}_\mathrm{l}$ as *auxiliary* variables indicating pure and lipidic fibrils that are not newly generated, i.e., such that $F_\mathrm{p} = \tilde{F}_p + F^*$ and $F_\mathrm{l} = \tilde{F}_l + F^*$. Edged arrows represent the reactions governing the dynamics of the system variables, including nucleation, elongation, structural conversions, and binding events, with the corresponding parameters. This model diagram presents a variable choice that relies on the distinction between number and mass concentrations. Green and pink boxes, together with supplementary circles, highlight pure protein and lipidic fibril species, respectively, whereas the gray box represents $M_{F,\mathrm{TOT}}$ as the union of $M_{F,\mathrm{p}}$ and $M_{F,\mathrm{l}}$. For simplicity of representation, we neglect the terms $k_\mathrm{on} V_\mathrm{b} M_{F^*}$ and $k_\mathrm{l1}\, m M_{F^*}$, involving the mass concentration of newly formed, pure protein, and lipidic fibrils. Note that there is no arrow between F^* and M_{F^*}, given that newly formed fibrils F^* transition to $\tilde{F}_\mathrm{p}$ upon elongation by monomer addition and do not grow in monomer count.

Methods section. As outlined in Table 1, M_A, M_B, M_{F^*}, $M_{F,\mathrm{p}}$, and $M_{F,\mathrm{l}}$ represent the concentration of monomers in oligomeric and fibrillar aggregates. In particular, we assumed that fibrils are the only species that can elongate by monomer addition at their ends, whereas oligomers, being nonfibrillar, are characterized by negligible elongation rate constant. This assumption results in the relationship $M_A = nA$ and $M_B = nB$. Such a coarse-grained representation of oligomer populations aligns with the kinetic modeling framework in Iljina et al.[30] and Dear et al.[31]. The limited contribution of oligomers to monomer consumption, as indicated by smFRET data[30], supports the assumption of a negligible oligomeric elongation rate constant compared to the dominant/driving process of fibril elongation. In our notation, $M_{F,\mathrm{p}}$ and $M_{F,\mathrm{l}}$ both include the mass concentration of newly generate fibrils $M_{F,*}$, with the differences indicated by $\tilde{M}_{F,\mathrm{p}}$ and $\tilde{M}_{F,\mathrm{l}}$, respectively. Therefore, the total mass concentration of fibrils $M_{F,\mathrm{TOT}}$ corresponds to the combined species concentration ($M_{F,\mathrm{p}}$ and $M_{F,\mathrm{l}}$) that accounts for the overlap (M_{F^*}), i.e., $M_{F,\mathrm{TOT}} = \tilde{M}_{F,\mathrm{p}} + \tilde{M}_{F,\mathrm{l}} + M_{F,*} = M_{F,\mathrm{p}} + M_{F,\mathrm{l}} - M_{F,*}$. Accordingly, the concentration of both fibrillar species includes the amount of newly generated fibrils, with $F_\mathrm{p} = \tilde{F}_\mathrm{p} + F^*$ and $F_\mathrm{l} = \tilde{F}_\mathrm{l} + F^*$, where $\tilde{F}_\mathrm{p}$ and $\tilde{F}_\mathrm{l}$ refer to pure protein and lipidic fibrils originating through F^* elongation and vesicle-F^* binding, respectively; and $F_{TOT} = \tilde{F}_\mathrm{p} + \tilde{F}_\mathrm{l} + F^* = F_\mathrm{p} + F_\mathrm{l} - F^*$.

These variables are interconnected through primary and secondary nucleation, oligomer conversion and dissociation, fibril formation, pure and vesicle-mediated fibril elongation, and monomer-vesicle binding, listed in Table 1. Reactions such as monomer-independent unimolecular oligomer structural conversions, oligomer dissociation, fibril formation, reversible monomer-vesicle binding, and pure fibril elongation are regulated by first- or second-order mass action rate laws. In contrast to homogeneous primary nucleation that cannot display saturation effects, heterogeneous primary nucleation involves a two-step enzymatic reaction catalyzed by various surfaces within the reaction vessel (e.g., the plate surface or the air-water interface concentration). To form oligomers A, monomers interact with a surface W according to the reaction:

$$n \cdot m + W \underset{k_{-\mathrm{p}}}{\overset{k_\mathrm{p}}{\rightleftarrows}} C_1 \overset{k_{\mathrm{cat,I}}}{\rightarrow} A + W \tag{1}$$

The corresponding Hill function $H(K_{\mathrm{max,I}}, K_\mathrm{P}, n)$ is defined as $k_{\mathrm{max,I}} \frac{m^n}{m^n + K_\mathrm{p}^n}$, with half-saturation constant $K_\mathrm{P} = (k_{-\mathrm{p}} + k_{\mathrm{cat,I}})/k_\mathrm{p}$. The maximal production rate is given by $k_{\mathrm{max,I}} = k_{\mathrm{cat,I}} W_\mathrm{TOT}$, where W_TOT, subsumed into the rate constant, represents the total concentration of surfaces catalyzing this reaction. Likewise, secondary nucleation involves a two-step catalytic reaction catalyzed by fibril surfaces S:

$$n \cdot m + S k_{-\mathrm{s}} k_\mathrm{s} \rightleftarrows C_2 \overset{k_{\mathrm{cat,II}}}{\rightarrow} A + S \tag{2}$$

The corresponding Hill function $H(k_{max,II}, K_\mathrm{S}, n)$ is given by $k_{\mathrm{max,II}} \frac{m^n}{m^n + K_\mathrm{S}^n} S$, where $K_\mathrm{S} = (k_{-\mathrm{s}} + k_{\mathrm{cat,II}})/k_\mathrm{s}$ represents the half-saturation constant, and $k_{\mathrm{max,II}} = k_{\mathrm{cat,II}}$ denotes the maximal production rate constant. Here, S is assumed to be proportional to fibril mass concentration. Specifically, in the model, secondary nucleation can occur on pure, lipidic, and newly generated fibril surfaces, which are assumed proportional to $\tilde{M}_{F,\mathrm{p}}$, $\tilde{M}_{F,\mathrm{l}}$, and $M_{F,*}$, respectively. The corresponding secondary nucleation rate constants are defined as $k^\mathrm{p}_{\mathrm{max,II}}$, $k^\mathrm{l}_{\mathrm{max,II}}$, and $k^*_{\mathrm{max,II}}$. When only one secondary nucleation mechanism is considered, the rate constant is indicated as simply $k_{\mathrm{max,II}}$. Note that assuming the same rate constant for different secondary nucleation mechanisms results in a corresponding flux proportional to the total fibril mass concentration, i.e., $k_{\mathrm{max,II}} \frac{m^n}{m^n + K_\mathrm{S}^n} M_{F,\mathrm{TOT}}$.

In lipidic environments, monomers reversibly bind to and dissociate from free vesicles in solution, regulated by a dissociation constant $K_\mathrm{D} = k^-/k^+$. This process contributes to the dynamic partitioning of monomers between the free and vesicle-bound states. The reversible binding is represented by a second-order mass action:

$$m + V_\mathrm{f} k^- k^+ \rightleftarrows m_\mathrm{b} \tag{3}$$

Here, $m_\mathrm{b} = \frac{M_\mathrm{s}}{\gamma} V_\mathrm{b}$, with M_s and γ denoting the lipid count of a vesicle (estimated to approximately 6000 lipids per SUV) and the number of lipids within a vesicle involved in binding to a protein monomer (estimated to ~30 lipids per protein), respectively[32]. The resulting monomer-coated vesicles V_b play a crucial role in fibril elongation by delivering both lipids and monomers to growing fibrils.

According to Dear et al.[16], lipid-mediated fibril elongation proceeds via a co-elongation mechanism: lipids are actively incorporated into the growing fibril structure during the elongation phase, rather than at the initial nucleation stages, and this process depends on the relative rates of protein and vesicle addition. Specifically, monomer-coated vesicles initially bind to fibril ends at rate constant k_on. As approximately γ monomers are sequentially added to fibrils at rate constant k_{l2}, these monomers intermix with lipids provided by vesicles to form lipid-protein co-aggregates, which thus do not result from pre-bound "lipidic monomers". While vesicle binding to fibril surfaces and monomer addition to fibril ends are reversible reactions, we assumed back reactions to be significantly slower than their corresponding forward reactions and thus negligible[16]. In particular, vesicles likely do not remain permanently bound to the fibril surface but stay temporarily to enable elongation, facilitating the formation of lipid-protein co-aggregates without requiring vesicle engulfment or disassembly. Given that the model focuses on the overall aggregation kinetics - not on tracking the precise dynamics of individual vesicles, the vesicle dynamics is simplified to a "delivery" model: upon γ monomers incorporation per binding event, a new vesicle needs to "dock" to the new growing end and "deliver" its cargo of lipids to further elongation, implying that the vesicle is no longer contributing to fibril growth. Therefore, the k_on constant effectively accounts for both vesicle binding and the delivery of lipids necessary for the process.

This mechanism is represented by a function depending on the amount of free monomers and monomer-coated vesicles, defined as:

$$f(\gamma, k_\mathrm{on}, k_{\mathrm{l2}}) = \gamma k_\mathrm{on} V_\mathrm{b} \frac{k_{\mathrm{l2}} m}{k_{\mathrm{l2}} m + \gamma k_\mathrm{on} V_\mathrm{b}} F_\mathrm{l} \tag{4}$$

where k_on and k_{l2} correspond to the rate constants of vesicle-fibril binding and lipidic fibril elongation by monomer addition, respectively. We assumed lipidic fibrils to elongate at the same rate constant as pure fibrils, i.e., $k_{\mathrm{l1}} = k_{\mathrm{l2}}$. This function has been recently proposed by Dear et al.[16], and a

Table 1 | Model variables and parameters

Model variables	
Variable name	**Symbol**
Monomer concentration	$\boldsymbol{m}$
Type-A oligomer concentration	$\boldsymbol{A}$
Type-B oligomer concentration	$\boldsymbol{B}$
Newly generated fibril concentration	$\boldsymbol{F^*}$
Pure fibril concentration	$\boldsymbol{F_p}$
Type-A oligomer mass concentration	M_A
Type-B oligomer mass concentration	M_B
Newly generated fibril mass concentration	$\boldsymbol{M_{F^*}}$
Pure fibril mass concentration	$\boldsymbol{M_{F,p}}$
Free vesicle concentration	$\boldsymbol{V_f}$
Monomer-coated vesicle concentration	$\boldsymbol{V_b}$
Fibril-bound monomer-coated vesicle concentration	$\boldsymbol{V_{F,b}}$
Vesicle-bound monomer concentration	m_b
Fibril-bound vesicle-coating monomer concentration	$m_{F,b}$
Lipidic fibril concentration	$\boldsymbol{F_l}$
Lipidic fibril mass concentration	$\boldsymbol{M_{F,l}}$
Total vesicle concentration	V_{TOT}
Total monomer concentration	m_{TOT}
Total fibril mass concentration	$M_{F,TOT}$
Model parameters	
Parameter name	**Symbol**
Number of monomers involved in nucleation	n
Rate constant for homogeneous primary nucleation	k_n
Maximum rate for heterogeneous primary nucleation	$k_{max,I}$
Nucleation equilibrium constant (heterogeneous)	K_P
Maximum rate constant for secondary nucleation	$k_{max,II}$
Nucleation equilibrium constant (secondary)	K_S
Rate constant for oligomer conversion	k_{c1}
Rate constant for oligomer dissociation	k_d
Rate constant for fibril formation	k_{c2}
Rate constant for pure fibril elongation	k_{l1}
Rate constant for lipidic fibril elongation	k_{l2}
Coefficient for vesicle-mediated fibril elongation	y
Rate constant for vesicle-fibril binding	k_{on}
Dissociation constant for monomer-vesicle binding	K_D
Backward rate constant for monomer-vesicle binding	k^-
Forward rate constant for monomer-vesicle binding	k^+
Number of lipids binding a monomer	γ
Average lipid count in vesicles	M_s

The bold variables are those included in the model equations, as reported in the "Material and methods" section.

more detailed description of its derivation is provided in the Material and Method section.

The model accounts for pure and lipidic aggregation routes by assuming shared initial aggregation and distinct elongation processes for the two fibrillar species. Specifically, on-pathway oligomers are assumed to be pure in both pathways, given the lack of detailed structural and mechanistic characterization of lipidic oligomers and the central role of lipid incorporation during the co-elongation phase of lipidic fibrils. While to our knowledge no mechanistic description of lipid-oligomer interactions is available in the literature to our knowledge, the existence of lipidic oligomers cannot be entirely excluded. According to Dear et al.[16], various protein-only and protein-lipid clusters develop during nucleation in the lipid vesicle experimental setup. While these clusters could be intermediates, the authors identified the nucleus by its co-aggregate nature and ability to grow into fibrils - i.e., as "the first species that structurally resembles the final aggregates and can rapidly grow through monomer addition" - rather than as an earlier-stage intermediate in the aggregation pathway. Therefore, early oligomerization may follow a protein-only pathway, with lipid incorporation becoming more prominent during fibril elongation. Building on these insights, our model focuses on monomer- and fibril-vesicle interactions as key reactions in lipidic fibril formation, reflecting the mechanistic emphasis on lipid incorporation at later stages rather than at early oligomerization or nucleation.

Figure 1a provides a graphical representation of the molecular mechanisms underlying our model, formalized by the diagram in Fig. 1b. Overall, the model of aSyn aggregation is based on a system of Ordinary Differential Equations (ODEs) describing the time evolution of monomer and aggregate levels. It consists of 12 ODEs, with 12 variables, 12 reactions, and up to 20 parameters (if we consider three distinct secondary nucleation mechanisms), and two algebraic equations corresponding to the conservation law of total monomer and vesicle concentrations, ensuring mass balance throughout the process. Table 1 lists the model variables and parameters; the highlighted variables appear in the model equations.

Integration of chemical kinetic model components. A detailed comparison between our work and other chemical kinetic models of aSyn aggregation[16,30–32,34,35] can be found in Supplementary Table 1 of the Supplementary Note 1, highlighting differences in mechanisms, variables, and reaction kinetics (e.g., mass action vs. catalytic processes). Chemical kinetic models often exclude intermediate species[19,34], focusing on nucleation-polymerization processes, or consider a single oligomeric state[32,35], facing limitations of data availability. Specific aSyn oligomers, however, play a crucial role in aggregation dynamics and cytotoxicity. Our model explicitly includes on-pathway oligomers undergoing structural conversion (from type-A to type-B), following the approach of Iljina et al.[30]. In addition, our model distinguishes between homogeneous and heterogeneous primary nucleation, in line with evidence suggesting distinct roles for these processes under specific experimental conditions; while homogeneous nucleation is required for initiating any aggregation process, heterogeneous nucleation is the dominant primary nucleation pathway for aSyn in many cases[16]. Although secondary nucleation is represented as a mass action process of order n, with $n < 1$ representing saturation, in many models[31,32,34,35], we explicitly represent it as a catalyzed reaction, where fibril surfaces - assumed to be proportional to fibril mass concentration - act as enzymes for type-A oligomer formation. For lipidic aggregation, our model incorporates the detailed aSyn-lipid interaction mechanisms described by Dear et al.[16] and includes explicit monomer-vesicle binding, moving beyond pre-equilibrium assumptions. While chemical kinetic models often focus on either pure or lipid-mediated aggregation, our approach acknowledges that both likely occur simultaneously in physiological environments, where aSyn interacts with various cellular co-factors and undergoes dynamic changes in its surroundings (e.g., pH shifts, variations in local lipid concentration, etc). Overall, our model uniquely integrates reaction types relevant to aSyn aggregation, from oligomer conversions and secondary nucleation to lipid interactions.

Context-dependent mechanisms of in vitro aSyn aggregation: model calibration and validation

The mechanisms involved in the model can contribute to the whole aggregation process to a different extent depending on the pathophysiological conditions of the surrounding environment. In in vitro aggregation assays, aSyn monomers in solution are resistant to nucleation, and specific catalysts are required to trigger their aggregation. The process can be accelerated or slowed down by different reactions depending on the nature of the initiating agents, physicochemical factors (e.g., pH, ionic strength, water activity), and solution conditions. For instance, the presence of lipid vesicles significantly boosts fibril elongation[16], whereas secondary nucleation dominates the

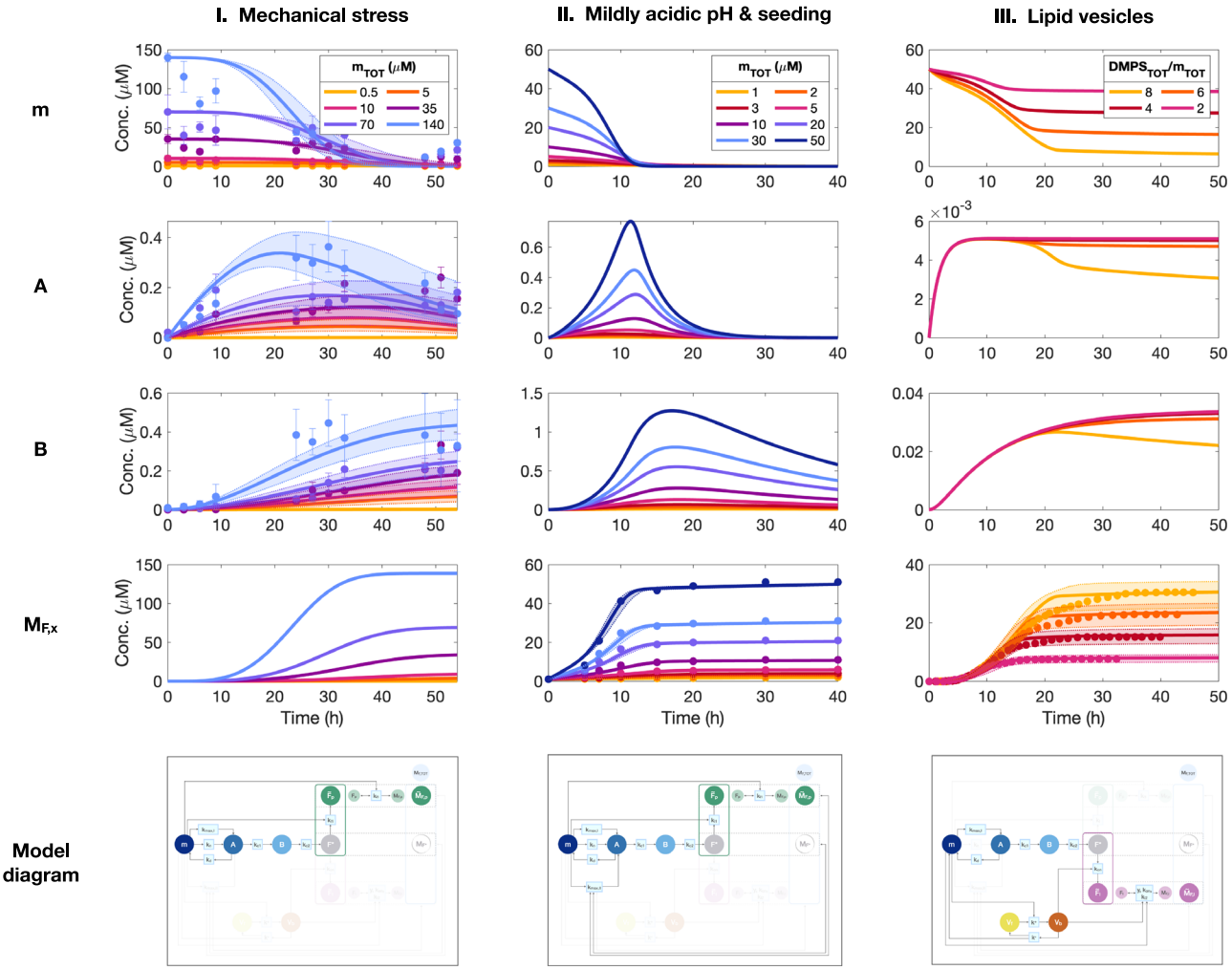

Fig. 2 | Calibration and validation of the model of pure and lipid-mediated aSyn aggregation on experimental data from in vitro aggregation assays of monomers in solution with different initiators. The three scenarios differ in terms of solution conditions and measurement techniques: **I**. Mechanical stress by constant agitation at 200 rpm, neutral pH, T = 37°, smFRET[30]; **II**. Mildly acidic pH (=5.5) and pre-formed fibril seeds ($M_{F,p}$ = 1 μM), quiescent solution, T = 37°, ThT dye fluorescence[34]; **III**. DMPS SUVs, quiescent solution, neutral pH, T = 30°, ThT dye fluorescence[32]. Here, ODE deterministic simulations (lines) represent the time evolution of monomer, oligomer, and fibril mass concentrations. Dots indicate the experimental data and bars the standard deviation, if available. Simulations are color-coded for different initial monomer levels, for the first two scenarios, and multiple lipid-to-aSyn ratios ($DMPS_{TOT}/m_{TOT}$), obtained by varying the lipid amount and keeping total monomer concentration fixed at 50 μM. Uncertainty quantification on the parameter estimates related to the best-in-fit was performed to produce lower and upper bands corresponding to the 5th and 95th percentiles of the simulations for the fitted variables. The model diagrams in the bottom row represent activated reactions in each calibration scenario, depending on the aggregation nature (pure vs. lipidic).

aggregation process as a result of pH variations and the addition of preformed fibril seeds[34]. This information has emerged from the rigorous analysis of aSyn aggregation kinetics[16,17,19,30,32,34,36]. To account for the significant variations in the contribution of each microscopic event, we calibrated and validated the model on different sets of published data from in vitro aggregation assays of recombinant purified aSyn[30,32,34]. Specifically, we considered four aggregation scenarios, three shown in Fig. 2 and the fourth in Fig. 3:

1. constant agitation of aSyn monomers with oligomer data obtained using single-molecule Förster Resonance Energy Transfer (smFRET) measurements[30];
2. pH variations from neutral to mildly acidic levels and inclusion of preformed fibrils seeds with Thioflavin-T (ThT) dye fluorescence data of pure aSyn fibrillation[34];
3. introduction of anionic phospholipidic vesicles, i.e., DMPS SUVs, in solution with monomers with a ThT-derived fibril mass dataset[32];
4. cytosolic ionic strength, neutral pH, and seeding with fibril and oligomer mass data obtained by ThT dye fluorescence and single-molecule fluorescence-free electrophoresis (FFE), respectively[35].

Although calibrating the model on smFRET-derived data obtained under mechanical stress provides valuable insights into aSyn oligomerization, there is a potential mismatch between constant agitation of monomers in solution and the initiating factors of aggregation in vivo.

To address this limitation, we incorporated more physiologically relevant scenarios; aSyn is predominantly cytosolic, where the pH ranges from 7.2 to 7.4, but also interacts with mildly acidic cellular compartments, such as intracellular vesicles, endosomes, and lysosomes, where a slightly lower pH can influence its aggregation dynamics. In this context, a shift from neutral to mildly acidic pH, coupled with the strong seeding of pre-formed fibrils, represents a physiologically relevant scenario. Similarly, the presence of lipid vesicles at varying lipid-to-aSyn ratios provides an additional layer of biological relevance, given the well-established role of membrane interactions in aSyn aggregation. Finally, to further account for physiological conditions mimicking the cellular environment, we extended our analysis to a dataset reflecting aggregation under cytosolic ionic strength and neutral pH[35].

The model allows for calibration with pure protein or lipidic fibrillation datasets. Under the experimental conditions of the lipid vesicle setup, pure

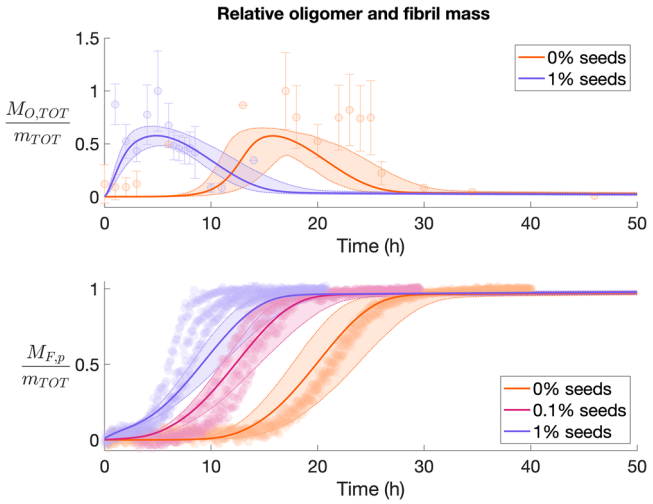

Fig. 3 | Quantitative analysis of aSyn aggregation kinetics under physiological solution conditions. Neutral pH (=7.4), quiescent solution, $T = 37^{\circ}$, cytosolic ionic strength, and varying preformed fibril seeds. Model simulations (solid lines) compared with experimental measurements (dots), i.e., total oligomer mass ($M_{O,TOT}$) and fibril mass ($M_{F,p}$), measured by single molecule microfluidics and ThT dye fluorescence, respectively, and normalized to total protein content $m_{TOT} = 100$ μM; low experimental accuracy of oligomer measurements indicated by the error bars (standard deviation) results from a yet-to-optimize protocol. Experimental data is obtained from Xu et al.[35]. Model calibration using combined fibril and oligomer mass measurements from 0% (orange) and 1% (purple) seeing conditions, showing oligomer dynamics with time-shifted peaks and corresponding fibril formation with distinct lag phases. Model validation with updated parameter estimates against fibril mass measurements for 0.1% (light pink) seeding conditions. Lower and upper bands constraining the shaded areas represent the 5th and 95th percentiles of the uncertainty quantification of the fitted variables. Updated parameter estimates are provided in Table 3.

protein fibrils do not form under these conditions, and lipidic fibrils are the main aggregation product[15,16]. Accordingly, when calibrating on lipid-mediated aggregation data, we deactivated pure aggregation. For all scenarios, the model was calibrated on data associated with the highest and lowest initial monomer, seeding conditions, and lipid-to-aSyn levels, and validated on the remaining time series. For effective calibration across multiple datasets, we implemented a step-wise approach guided by data availability and biological knowledge, as detailed in the Material and Methods section. Parameter estimation followed two main principles: (i) for reactions consistently shared with existing models (such as standard and lipid-induced fibril elongation and oligomer dissociation), we maintained literature-derived values; (ii) the remaining parameters, including rate constants for oligomeric conformational changes and nucleation mechanisms, were estimated. To address data limitations, particularly the lack of oligomer measurements across different scenarios, we applied additional constraints such as maintaining fixed ratios between oligomer conversion rates, derived by calibration on available oligomer data from shaking-induced aggregation[30]. The resulting parameter estimates are shown in Tables 2 and 3. When the comparison is feasible in terms of unit of measure, our parameter estimates align with previously published values while extending the model applicability across diverse experimental conditions (see Supplementary Table 2). In addition, we performed uncertainty quantification on the parameter estimates related to the best fit to assess whether the model design is flexible enough to reflect the entire variability expressed by the data while retaining a meaningful and interpretable parametrization.

The model recapitulates critical aspects of aSyn aggregation dynamics across diverse in vitro scenarios

The resulting model simulations against experimental data are shown in Fig. 2, with the corresponding parameter estimates in Table 2. Fibril mass concentration exhibits the characteristic sigmoidal profile, identified by an initial lag phase, followed by a growth phase due to increased monomer-to-fibril conversion until a plateau is reached, usually due to monomer depletion. This curve shows a propensity for faster monomer addition to existing aggregates rather than de novo oligomer formation.

Table 2 | Parameter estimates derived from a step-wise model calibration procedure on data from in vitro aggregation assays of recombinant purified aSyn under various conditions: (a) mechanical stress through constant agitation, (b) a shift in pH from neutral to mildly acidic & preformed fibril seeds, and (c) the presence of lipid vesicles, as detailed in the main text and shown in Fig. 2

(**a**) Mechanical stress

Parameter	Estimates	Unit
n	2	unitless
k_n	1.21e-06	$\mu M^{-1}\ h^{-1}$
$k_{max,I}$	6.32e-03	$\mu M\ h^{-1}$
K_P	5.25	μM
k_d	2.4e-03[3,31]	h^{-1}
k_{c1}	4.28e-02	h^{-1}
k_{c2}	7.33e-03	h^{-1}
k_{l1}	7.92[36]	$\mu M^{-1}\ h^{-1}$

(**b**) Mildly acidic pH & seeding

Parameter	Estimates	Unit
n	2	unitless
k_n	1.21e-06	$\mu M^{-1}\ h^{-1}$
$k_{max,I}$	6.32e-03	$\mu M\ h^{-1}$
K_P	5.25	μM
$k_{max,II}$	7.89e-03	h^{-1}
K_S	2.13	μM
k_d	2.4e-03[3,31]	h^{-1}
k_{c1}	2.76e-01	h^{-1}
k_{c2}	4.13e-02 (= 1.5e-01 k_{c1})	h^{-1}
k_{l1}	7.92[36]	$\mu M^{-1}\ h^{-1}$

(**c**) Lipid vesicles

Parameter	Estimates	Unit
n	2	unitless
$k_{max,I}$	3.09e-03	$\mu M\ h^{-1}$
K_P	5.25	μM
k_d	2.4e-03[3,31]	h^{-1}
k_{c1}	5.91e-01	h^{-1}
k_{c2}	8.86e-02 (= 1.5e-01 k_{c1})	h^{-1}
k_{l2}	7.92[36]	$\mu M^{-1}\ h^{-1}$
y	457.5	unitless
k_{on}	7.52e01	$\mu M^{-1}\ h^{-1}$
K_D	3.8e-01[32]	μM
k^-	1.63e-03	h^{-1}
k^+	4.30e-03	$\mu M^{-1}\ h^{-1}$
γ	3e01[32]	unitless
M_s	6e03[32]	unitless

We assumed a fixed size for oligomers, setting the parameter n to 2 as in the literature[55]. Fitted parameters in each scenario are highlighted in light blue. Following a step-wise approach, the parameters highlighted in gray are carried over from the model calibration of the previous scenario (from left to right). The remaining parameters are fixed to literature values; those without a reference are derived from relationships defined in the literature, as detailed in the Material and Methods section.

Table 3 | Parameter estimates derived from model calibration on aSyn aggregation data obtained under physiological solution conditions, as reported by Xu et al.[35]

Parameter	Estimates	Unit
n	2	unitless
k_n	1.21e-06	$\mu M^{-1}\,h^{-1}$
$k_{max,II}$	6.32e-03	$\mu M\,h^{-1}$
K_P	5.25	μM
$k_{max,II}$	**6.67**	**h^{-1}**
K_S	**44.40**	**μM**
k_d	1[35]	h^{-1}
k_{c1}	**8.67e-03**	**h^{-1}**
k_{c2}	**1.71e-02**	**h^{-1}**
k_{l1}	7.92[36]	$\mu M^{-1}\,h^{-1}$

Fitted parameters are highlighted in bold. Corresponding model simulations are shown in Fig. 3.

As shown in the second scenario, the presence of preformed fibrils can bypass primary nucleation. As the pH becomes acidic, the estimated rate constant for secondary nucleation exceeds the rate constants associated with primary nucleation reactions, underscoring the significance of secondary nucleation in driving the aggregation process[34]. An increase in the preexisting fibril seed level or the total monomer level (while maintaining the same initial concentration of fibrils) leads to a faster overall aggregation reaction. Conversely, the initial lag phase is prolonged when aggregation is initiated not by the presence of aggregates but by other factors, such as mechanical stress or lipidic vesicles. Furthermore, our model reproduces fibrils with average lengths consistent with in vitro experimental data across different aggregation scenarios (see Supplementary Note 2 and Supplementary Fig. 1).

The lipidic environment considered for model calibration involves intermediate lipid-to-protein ratios, corresponding to a surplus of free aSyn monomers over the amount that saturates the vesicle membranes. The relative proportion of lipids to monomers significantly affect the aggregation kinetics. These specific conditions promote the formation of amyloid fibrils, where the experimental plateau levels scale linearly with lipid concentration[32]. Our model captures this feature and other critical aspects of lipidic aSyn aggregation, owing to the specific formulation of the flux associated with vesicle-mediated fibril elongation (see eq. (4))[16]. Indeed, the dual dependence of the rate of lipid-mediated fibril elongation on both the concentrations of monomer-coated vesicles and free monomers triggers a rapid transition in the rate of fibril formation within the specified time interval and across the majority of initial lipid-to-aSyn ratios. This transition results from a shift in the rate-limiting step of aggregation, moving from protein-dependent to lipid-dependent kinetics. In the following section, we provide the specifics of this case and discuss the broader implications.

In both pure protein and lipidic aggregation pathways, the structural conversion reactions between oligomeric and fibrillar species are crucial steps. The smFRET method predominantly detects stable oligomers, which persist throughout the aggregation pathway. Therefore, by fitting smFRET-derived oligomer data from a shaking-induced aggregation assay, our model effectively captures the dynamics of these long-lived oligomers. In particular, model simulations can grasp the sequential nature of stable oligomers: type-A oligomer concentration reaches the peak before type-B oligomers, confirming that both oligomeric types are on-pathway. In the lipid-rich environment, the sequential order of oligomeric peaks is maintained, albeit with a delayed peak time. On the other hand, the oligomeric abundance decreases by two orders of magnitude compared to scenarios of pure protein aggregation. According to our model calibration on oligomer data[30], the conformational change from type-B oligomers to fibrils is one order of magnitude slower (i.e., $k_{c2}/k_{c1} = 0.15$) than fast conversion between the two oligomeric species. Assuming that the ratio k_{c2}/k_{c1} is maintained across all aggregation scenarios, our model implied that the rates of oligomer structural conversion increase substantially to capture the observed fibril growth profile in the second and third scenarios (see Table 2).

Providing mechanistic insights into secondary nucleation and oligomer nature in physiological conditions. Recent work by Xu et al.[35] introduced an in vitro aggregation assay that mimics the cellular environment by maintaining neutral pH and cytosolic ionic strength across various seeding scenarios. Our model, originally calibrated under mildly acidic conditions, successfully captured fibril mass concentration-time profiles for intermediate-to-high seeding, i.e., 1% and 10% seeds, but showed limitations at low seeding, i.e., 0% and 0.1% seeds (see Supplementary Fig. 2). This validation suggests that cytosolic ionic strength likely governs aggregation initiation at low seed concentrations, whereas preformed fibrils are the primary catalysts of aggregation at higher seeding levels. Indeed, robust performance of the model in higher seeding scenarios stems from its calibration dataset, which spans seeding levels from 2% to 100% (1 μM preformed fibril mass, 1 - 50 μM initial monomer concentration). These results indicate that secondary nucleation parameters remain reasonably constrained across varying pH conditions when sufficient seeds are present. While pH strongly modulates secondary nucleation rates under low seeding conditions as previously shown[36], the effect of pH on this mechanism becomes less critical due to the high local concentration of catalytic surfaces.

Oligomers reported in Xu et al.[35], on the other hand, showed substantially higher abundance (45 to 65-fold increase) and faster dissociation rates (hours versus days) compared to those in Iljina et al.[30], which provided the initial calibration data. This discrepancy stems from fundamental differences in detection methods rather than solution conditions (see Supplementary Fig. 2 and Supplementary Table 3 in Supplementary Note 3). While offering detailed insights into stable oligomers, traditional smFRET is limited by sample dilution, which hampers the detection of transient species. In contrast, newer minimally perturbative techniques, such as single-molecule microfluidics[35], preserve oligomer equilibrium and capture fleeting, transient species. These methods may detect either transient species or the total oligomer population, of which stable oligomers represent a small fraction.

Since the model was initially calibrated on smFRET-derived data, it specifically captures the dynamics of long-lived oligomers. To account for short-live oligomers observed under native-like conditions, we recalibrated the model using combined fibril and oligomer mass time-concentration profiles for 0% and 1% seeded aggregation (see the Materials and Methods section for further details). The model fitted both fibril and oligomer kinetics for 0% and 0.1% seeds and was able to reproduce the the fibril mass profile for 0.1% seeding conditions, as shown in Fig. 3 and Supplementary Fig. 3. Notably, the updated secondary nucleation and oligomer dissociation rate constants reached comparable magnitudes, indicating a balance between oligomer formation and dissociation into monomers under physiological conditions. This result confirmed secondary nucleation as the primary source of aSynoligomer formation[35]. Moreover, removing the prior constraint on oligomer conversion rates (i.e., $k_{c2}/k_{c1} = 0.15$), previously established for long-lived species, revealed that fibril formation outpaces inter-oligomer conversion in short-lived oligomers (i.e., $k_{c2}/k_{c1} \sim 2$).

A virtual lab for in silico experiments

Our model provides a computational environment for running a broad spectrum of in silico experiments, enabling the prediction and validation of hypotheses that underpin experimental investigations. In particular, it can provide insights into the interplay between pure protein and lipidic pathways and suggest target mechanisms to counteract aggregation.

Reproducing the impact of lipid-to-aSyn ratio on the dynamics of lipidic aggregation. As highlighted in the literature[16,32] and confirmed in the model calibration phase, the lipid-to-aSyn ratio R (i.e., $DMPS_{TOT}/m_{TOT}$ here) is a crucial control parameter for in vitro lipidic aSyn aggregation. While the calibration step focused on intermediate ratios,

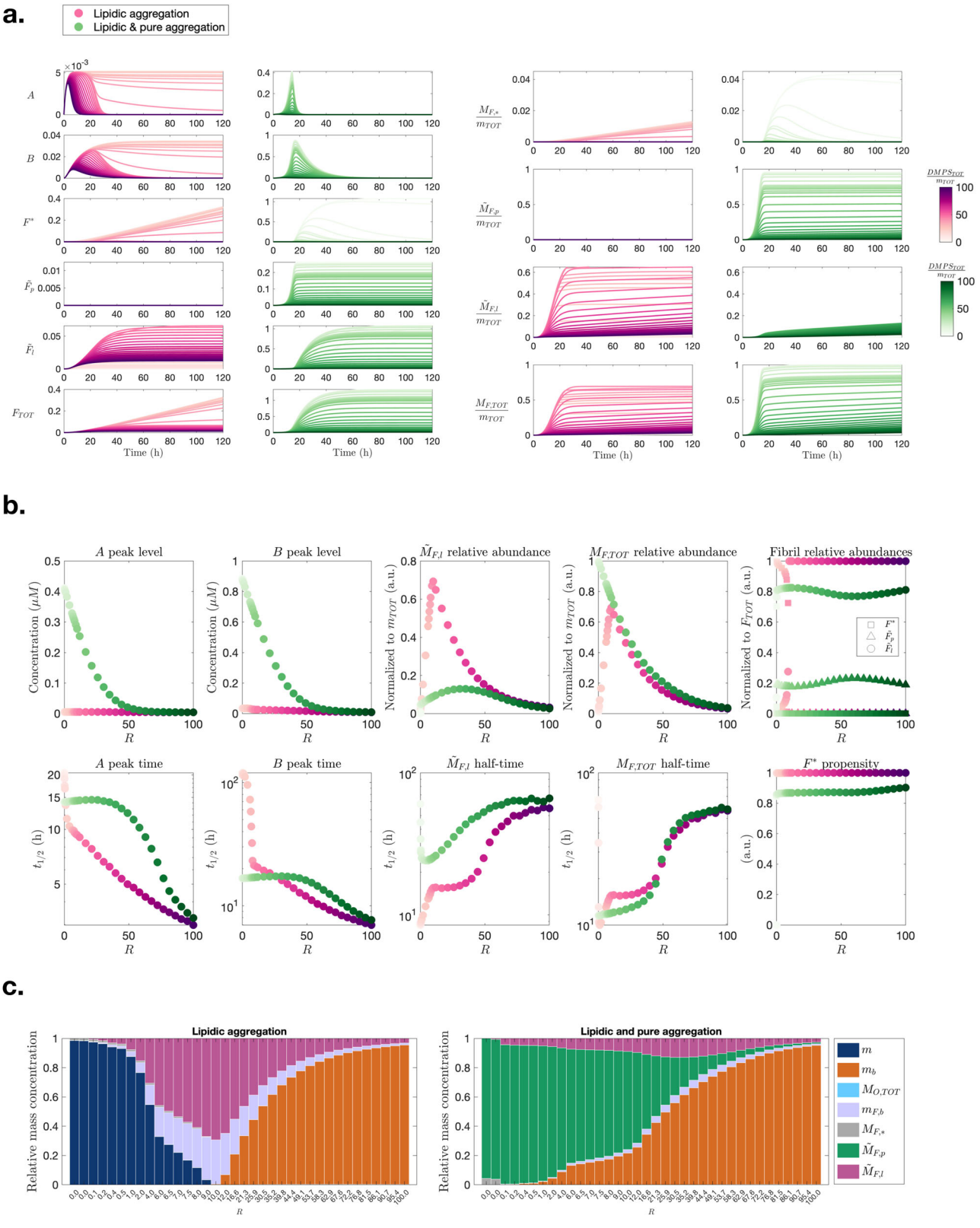

the model can be used to expand the analysis to a wider range of initial conditions, from surplus of monomers to excess of vesicles, thus providing predictions to be tested in vitro.

As shown in Fig. 4 (column 1 - pink/purple curves and points), our model faithfully reproduces the dynamics of lipidic aggregation, which was first experimentally observed by Galvagnion et al.[32] and more recently analyzed in mechanistic terms by Dear et al.[16]. The system includes the reversible binding between lipidic vesicles and free monomers, which is faster than fibril formation[16,32]. Therefore, an excess of lipids in the solution at the beginning results in lipid-bound monomers and a minimal amount of free monomers left for aggregation. Vice versa, a significant excess of monomers over lipids underlies an insufficient amount of monomer-coated

Fig. 4 | The impact of varying lipid-to-aSyn ratios on pure and lipidic aggregation. Pink and green shades denote lipid-mediated aggregation in isolation and in combination with pure protein aggregation, respectively. Concentrations (μM), time (hours). R represents the initial lipid-to-aSyn ratio (i.e., $DMPS_{TOT}/m_{TOT}$). **a** Deterministic simulations of aSyn oligomer and fibril formation (number and mass concentrations) under varying lipid concentrations ($DMPS_{TOT}$) with a fixed initial monomer concentration $m_{TOT} = 50\ \mu M$. Column one represents simulations with pure aSyn aggregation turned off, while column two depicts simulations with both pathways active, assuming equal rate constants for pure protein and lipidic fibril formation ($k_{l1} = k_{l2}$) and active secondary nucleation on pure fibrils ($k^{P}_{max,II} \neq 0$); **b** metrics including oligomeric peak time and level, lipidic and total fibril abundance (normalized to m_{TOT}) and half-times, fibril number concentrations at $t_f = 120$ h (normalized to F_{TOT}), and propensity for lipidic aggregation over pure protein aggregation; peak times and half-times are in log scale. Each point corresponds to a deterministic simulation colored according to the subplot above, with simulations ending at $t_f = 120$ h; **c** relative mass concentration of aSyn species in the model, i.e., (free and bound) monomer concentration and oligomer and fibril mass concentrations (normalized to m_{TOT}).

vesicles to enable the elongation of lipidic fibrils by monomer addition, thus inhibiting aggregation. Notably, in this case, oligomers persist longer and primarily give rise to newly generated fibrils, which become the dominant aggregate type as the scarcity of lipidic vesicles prevents their elongation into fibrils (Fig. 4a, column 1). These behaviors arise from an unbalance between free and vesicle-bound monomers. Conversely, when the concentrations of the two species are balanced such that there is a surplus of monomers over the amount that saturates the lipidic vesicles, the system induces aggregation. Specifically, lipidic fibrils increase linearly in both number and mass concentrations with increasing total lipid concentrations, but only up to a certain lipid-to-protein ratio ($DMPS_{TOT}/m_{TOT} \sim 10$ in our simulations with 50 μM aSyn monomers and 100 to 5000 μM DMPS vesicles). Beyond this threshold, lipidic aggregation drops. The third scenario used for model calibration falls within this latter case of intermediate lipid-to-aSyn ratios.

While the lipidic aggregation rate is initially determined by the flux related to type-B oligomer conversion, it can be reasonably approximated by the flux term related to vesicle-mediated fibril elongation[16] at prolonged times. This reaction rate depends on the availability of free monomers and monomer-coated vesicles. Following the work of Dear et al.[16], we can identify two regimes: (i) when bound vesicles are in excess over free monomers ($y k_{on} V_b \gg k_{l2} m$), the lipidic aggregation rate is limited by free monomer concentration and, thus, the plateau level is reached upon monomer depletion. Conversely, (ii) in the case of free monomer excess over bound vesicles ($y k_{on} V_b \ll k_{l2} m$), the lipidic aggregation rate is limited by the availability of monomer-coated vesicles, and the fibril mass concentration stabilizes at a plateau level upon vesicle depletion. Here, the plateau of lipidic fibril mass concentration $\tilde{M}_{F,l}$ scales linearly with total lipid concentration, being defined by the number of free monomers added to fibril ends upon vesicle binding y and the total vesicle concentration V_{TOT}, with no dependence on the initial monomer concentration, in agreement with experimental results[32]. Unlike pure protein aggregation, a certain amount of free monomers remains in solution instead of being incorporated into fibrils. Moreover, the monomer count of newly generated fibrils significantly contributes to the total fibril mass concentration in the lipid-limiting regime, whereas it is nearly zero in the monomer-limiting regime.

The switch from protein-dependent to lipid-dependent kinetics occurs for $V_b/m = y^{-1} k_{l2}/k_{on}$, when the concentration of bound lipids is approximately 1.4 times the free monomer level, given the parameter estimates in Table 2. Whether this transition in the rate of fibril formation takes place depends on the initial lipid-to-protein ratio. Since our model explicitly describes monomer-vesicle binding, without a pre-equilibrium assumption, a short initial time interval exists during which monomer-coated vesicles are not yet formed in the deterministic simulations, thus $k_{l2} m \gg y k_{on} V_b$. This condition persists throughout the experiment, resulting in a lipid-limiting regime for low lipid-to-protein ratios, corresponding to an excess of monomers over lipids. Conversely, high lipid-to-protein ratios trigger and sustain the reverse condition ($k_{l2} m \ll y k_{on} V_b$), as bound vesicles significantly outnumber free monomers. Finally, intermediate lipid-to-protein ratios lead to an initial transition from the lipid- to the protein-limiting regime, followed by a shift back to the lipid-limiting kinetics, all within the same experimental time frame.

Exploring the interplay of pure and lipidic aggregation in response to varying lipid-to-aSyn ratios. Under physiological conditions, aSyn likely undergoes both aggregation routes simultaneously. The propensity for one pathway over the other depends on various cellular co-factors and conditions, with lipid-to-aSyn ratio possibly playing an important regulatory role. For example, in response to endosomal sorting, recycling pathways, and environmental factors, cellular environments such as synaptic vesicles or endosomal compartments may experience fluctuations in local vesicle and protein concentrations, which could disrupt the fine-tuned balance between beneficial and detrimental aSyn-lipid interactions. A mechanistic understanding of the response of aggregation system responds to these perturbations is therefore crucial. In this regard, our model provides an in silico framework to elucidate how varying lipid-to-aSyn ratios influence the interplay between pure and lipidic aggregation.

The previous scenario, based on the experimental setup with lipidic vesicles used for model calibration, represented an idealized case where pure protein fibrils do not form[16,32] (see Fig. 4c). Indeed, the pure aggregation pathway was entirely suppressed by imposing a strict constraint on fibril elongation ($k_{l1} = 0$), preventing newly generated and pure fibrils from elongating via monomer addition and ensuring that all fibrillar products contain lipids. This analysis underscored the critical role of the lipid-to-aSyn ratio in regulating lipidic aggregation and driving distinct kinetic regimes. To explore how these dynamical and steady-state features of lipidic aggregation translate into a more physiologically relevant scenario - where pure and lipidic aggregation occur simultaneously - we extended the previous scenario by relaxing the constraint on pure fibril elongation (i.e., $k_{l1} = k_{l2}$). In addition to enabling pure fibril growth, this modification introduces new fibril surface areas that promote oligomer formation, triggering a positive feedback loop via secondary nucleation with rate constant $k^{P}_{max,II}$: oligomers, in turn, convert into newly generated fibrils, amplifying both pure and lipidic fibril formation due to their shared aggregation route. Figure 4 shows the comparison between lipidic aggregation combined with pure protein aggregation (in green) and lipidic aggregation in isolation (in pink), in terms of dynamics and specific aggregation metrics (detailed in the Material and Methods section). In particular, Fig. 4c shows the relative mass of aSyn species - and system variables - at the final simulation time ($t_f = 120$). We performed an additional analysis to disentangle the effects of pure and lipidic elongation within the full aggregation system by excluding secondary nucleation mechanisms from both pathways. As shown in Supplementary Fig. 5 and Supplementary Note 4, the fundamental insights not specifically related to secondary nucleation remain unchanged.

In the absence of lipidic vesicles ($R = 0$), pure fibrillation is the only viable pathway. Newly generated fibrils cannot transition into lipidic fibrillar species but can elongate via standard monomer addition, forming pure fibrils. Therefore, in contrast to lipidic aggregation alone, oligomers appear transiently even at low lipid-to-protein ratios. Moreover, the availability of new fibril surfaces triggers the secondary nucleation flux (proportional to $\tilde{M}_{F,p}$), significantly increasing oligomer abundance. Oligomer peak levels are highest in the absence of lipidic vesicles and decreases as the lipid-to-monomer ratio rises, eventually matching levels observed when only lipidic aggregation occurred, with no secondary nucleation assumed. Conversely, at high lipid-to-monomer ratios ($R > 50$), both pure and lipidic pathways are inhibited due to monomer sequestration by lipids. Most monomers bind to vesicles, leaving minimal free monomers for either pathway. The remaining free monomers are divided between pure and lipidic fibril formation as conditions allow, leading to similar system behavior regardless of aggregation mode (lipidic pathway alone or combined).

At intermediate R, the system exhibits a competitive environment where pure and lipidic pathways influence each other kinetics and steady-

state behavior. As lipidic vesicles are introduced, monomers initially bind vesicles before being depleted via pure and lipidic elongation. Increasing R reduces pure fibril mass concentration ($\tilde{M}_{F,\mathrm{p}}$) while favoring lipidic fibrils ($\tilde{M}_{F,\mathrm{l}}$) and monomer-coated vesicles - free or bound to fibrils (m_{b} or $m_{F,\mathrm{b}}$), as described by Fig. 4c. Eventually, the system mirrors lipidic aggregation alone as previously discussed. Despite reduced mass concentration across all ratios, the qualitative behavior of lipidic fibrils ($\tilde{M}_{F,\mathrm{l}}$ and $\tilde{F}_{\mathrm{l}}$) remains consistent with previous findings. When lipidic aggregation occurs in isolation, lipidic fibril mass and number concentrations increase linearly with total lipid concentration until a threshold ($R \sim 10$), beyond which aggregation declines. When pure and lipidic aggregation coexist, a scaled yet non-linear increase in lipidic fibril mass and number concentrations was observed at plateau, peaking at $R \sim 30$ before declining due to monomer depletion caused by vesicle excess. Figure 4c (right) shows the remaining monomers distribute between pure fibrils and vesicle-bound monomers, with proportions varying by lipid-to-aSyn level. Overall, incorporating pure aggregation into the system shifts lipidic aggregation thresholds and breaks robustness of the plateau of lipidic fibril mass $\tilde{M}_{F,\mathrm{l}}$ to variations in initial monomer levels (see Supplementary Fig. 4) but does not blur the distinction between lipid- and protein-limiting kinetic regimes.

As shown by Fig. 4b, total fibril mass ($M_{F,\mathrm{TOT}}$) decreases monotonically from m_{TOT} (pure protein aggregation) as lipid concentration increases. This reflects an initial dominance of pure fibrils, followed by a balance between pure and lipidic fibrils at higher lipid concentrations, with unincorporated monomers accumulating due to vesicle surplus. Notably, newly generated fibrils strongly favor lipidic aggregation, even at low lipid-to-monomer ratios, reaching nearly 90% propensity for the lipidic pathway at high R. This trend is observed in fibril number concentrations (see Fig. 4b). In particular, the switch from pure to lipidic dominance at very low R results from secondary nucleation, which enhances pure as well as lipidic aggregation due to their shared early-stage processes. As detailed in the Material and Methods section, we derived measures that quantify Lewy body composition. These indexes - albeit artificial in vitro conditions - can provide a system measure of the interplay of aggregation pathways. In combined aggregation (see Supplementary Fig. 6), the system consistently forms heterogeneous Lewy body-like inclusions across most lipid-to-aSyn ratios (except at very low ones), characterized by limited pure fibril derivation (I^{p} up to 6%) and up to 66% lipidic fibril derivation (I^{l}), alongside significant cross index contribution (I^{cross}).

In silico-aided therapeutic strategies informed by local sensitivity analysis. Mechanistic insights into aSyn aggregation can be crucial in guiding the development of Parkinson's disease therapies. What is the ideal mechanism of action for small molecules targeting aSyn aggregation? Which reactions should be perturbed by candidate compounds? Our model of pure and lipid-mediated aSyn fibrillation allows to investigate the effect of therapeutic strategies that affect both aggregation routes, tuning their effect to maximize their efficacy potential.

As previously discussed, our model assumes the overlap between pure and lipid-induced pathways at the initial steps of aggregation, until elongation mechanisms differentiate between pure and lipidic fibrils. Another assumption involved secondary nucleation mechanisms. Evidence for secondary nucleation in lipid-induced aggregation is significantly weaker than in pure protein aggregation[16,32]. Accordingly, we suppressed it when calibrating the model for lipidic aggregation at intermediate lipid-to-aSyn ratios. However, given the limited fibril surface exposure due to bound vesicles, secondary nucleation rate is likely reduced - not negligible - in the lipidic pathway. To analyze the impact of secondary nucleation on the interplay between pure and lipidic aggregation, we differentiated between two secondary nucleation rate constants for pure and lipidic aggregation ($k^{\mathrm{p}}_{\mathrm{max,II}}$ and $k^{\mathrm{l}}_{\mathrm{max,II}}$, respectively). We assumed $k^{\mathrm{l}}_{\mathrm{max,II}}$ to be one order of magnitude slower than $k^{\mathrm{p}}_{\mathrm{max,II}}$ and newly generated fibrils, shared between the two pathways, to be too short to provide sufficient surface area for oligomer formation (i.e., $k^{*}_{\mathrm{max,II}} = 0$). A more refined approach could scale the lipidic contribution to the secondary nucleation flux according to the reduced accessible surface area dictated by vesicle binding ($< \tilde{M}_{F,\mathrm{l}}$). To analyze the impact of secondary nucleation and the other aggregation mechanisms on the cross-talk between pure and lipidic pathways, we relied on the second parameter combination for pure protein aggregation (see Table 2), reflecting a mildly acidic pH scenario where all nucleation reactions contribute to the process to some extent, and on the third set of parameter estimates for lipidic aggregation.

As shown by Fig. 5, we performed a local sensitivity analysis (LSA) to quantify the impact of model parameters on relevant aSyn species through the AUC-based sensitivity index (SI) defined in the Material and Methods section. The sensitivity of each parameter is indicated by the distance of its corresponding point from the center of the figure. Here, we also explored the impact of initial conditions, i.e., the presence or absence of aggregates, on parameter sensitivity. For most parameters, such variations either have a minimal effect on the outcome or corroborate the trend observed in the sensitivity ranking from the alternative scenario. As expected, the rate constants of oligomer conversions k_{c1} and k_{c2} mainly affect oligomer and pure fibril kinetics. Moreover, when considering type-A and type-B oligomers, as well as lipidic fibrils in terms of number and mass concentration, our model identifies the rate constant of secondary nucleation on pure fibrils $k^{\mathrm{p}}_{\mathrm{max,II}}$ as one of the most sensitive parameters. Interestingly, variations in this parameter significantly influence lipidic fibrils but do not affect pure fibril levels. In general, alterations of other parameters only marginally affect the monomer count of pure fibrils. Conversely, no variable seems to be affected by perturbation of secondary nucleation lipidic rate constant $k^{\mathrm{l}}_{\mathrm{max,II}}$. Another relevant parameter is the rate constant associated with pure fibril elongation k_{l1}, which consistently ranks among the top three sensitive parameters across relevant aSyn species, such as pure and lipidic fibrils and oligomers in terms of number concentration. In contrast, lipid-mediated fibril elongation rate constant k_{l2} counts among the insensitive parameters, even for the lipidic species.

Relying on these results, we simulated the impact of potential compounds targeting the most sensitive reactions by varying the corresponding model parameter. The LSA-informed model can virtually explore how significant variations of the most sensitive parameters (up to 50%) affect the dynamics and features of aSyn oligomers and fibrils throughout the aggregation process. Metrics such as type-B oligomer peak level and time, as well as pure protein and lipidic fibril abundances and half-times, can be seen as gauges of the toxicity level of the aggregation process. Even though the specific mechanisms of toxicity associated with aSyn aggregation are not fully understood, experimental evidence pointed to the inherent toxicity as well as seeding and spreading abilities of the aggregates as structural and functional drivers of the overall toxicity[5,37]. In particular, small fibril fragments have been suggested as primary spreading agents in PD because of their high seeding efficiency and internalization ability[30,38]. On the other hand, type-B oligomers have been identified as the most cytotoxic species due to their high β-sheet content[3,5].

Parameters such as k_{c1}, k_{c2}, and $k^{\mathrm{p}}_{\mathrm{max,II}}$ are crucial as they directly control oligomer concentrations. In particular, as suggested by LSA and shown in Fig. 5b, c, a 50% inhibition of secondary nucleation catalyzed by pure fibrils leads to significant changes in oligomer and fibril dynamics. Specifically, this perturbation reduces the oligomeric peak time while lowering the peak level of type-A and type-B oligomers by 40% and 20%, respectively. Given the high toxicity of type-B oligomers, e.g., linked to increased levels of ROS, this intervention could mitigate the harmful impact of aSyn aggregation. The effect of this inhibition on fibrils is less straightforward. As shown in Fig. 5c, under nominal parameter conditions, the system is characterized by a highly lipidic fibrillar content (~80% of total fibril concentration) and a strong propensity for lipidic over pure protein aggregation. Conversely, perturbing secondary nucleation only marginally affects these metrics. In particular, halving the rate constant $k^{\mathrm{p}}_{\mathrm{max,II}}$ decreases both lipidic and pure fibril concentrations ($\tilde{F}_{\mathrm{l}}$ and $\tilde{F}_{\mathrm{p}}$). This results in a slight reduction in lipidic aggregation propensity while promoting a significant increase in pure fibrillar content - though not enough to overturn lipidic dominance. In terms of monomer counts, total fibril mass concentration shows a minimal overall loss (under 0.03% to 50% inhibition), driven by a

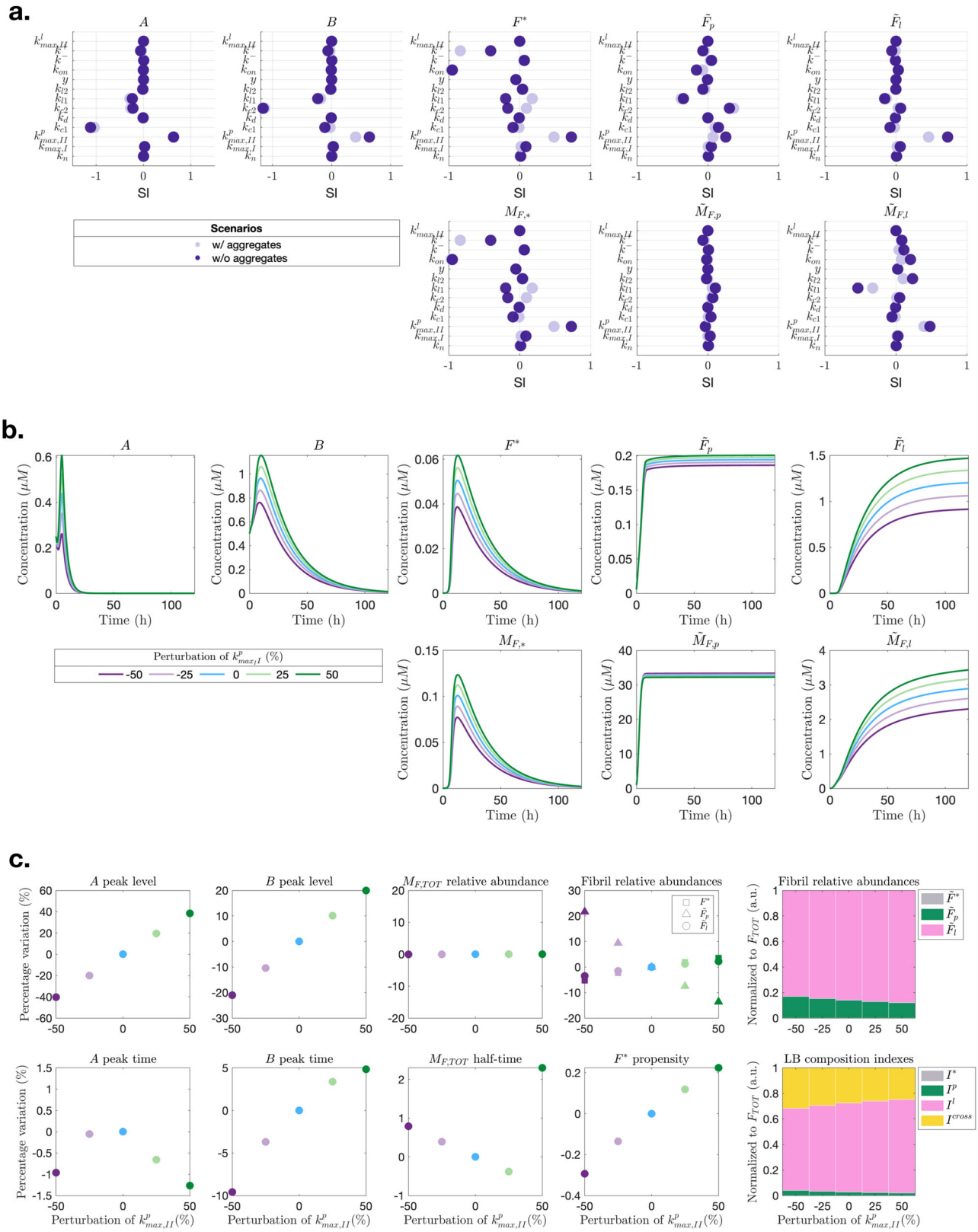

Fig. 5 | Local sensitivity analysis-informed modeling of the effect of anti-aSyn aggregation drugs. a Relative AUC-based sensitivity index corresponding to the 1% perturbation of each rate constant. Different colors correspond to different initial concentrations: absence (dark) and presence (light) of aggregates at $t = 0$, i.e., $m = 35\,\mu M$, $\tilde{M}_{F,\mathrm{p}} = 1\,\mu M$, and $M_A + M_B = 4\%\ m_{\mathrm{TOT}}$. **b** Deterministic simulations representing the variations in the model dynamics in response to perturbations of the secondary nucleation rate constant $k^{\mathrm{p}}_{\mathrm{max,II}}$, up to 50% of the nominal level; **c** Percentage variation of specific metrics describing the dynamics and features of oligomers and fibrils throughout the aggregation process. Each point is associated with the deterministic simulation of the corresponding color in the subplot above, with final time $t_f = 120$ h.

small increase in pure fibrils counterbalanced by a significant decrease in lipidic fibrils. In summary, while strong inhibition of secondary nucleation favors pure fibril formation, it is insufficient to substantially reduce overall lipidic contributions, as also reflected in Lewy body composition indexes.

Discussion

By elucidating the dynamics of pure and lipid-mediated aSyn aggregation in diverse environments, our model offers a unified representation of specific mechanisms underlying PD pathogenesis. Our work is grounded in insights mainly provided by the chemical kinetic models[16,17,19,20]. Tailored on ad-hoc test-tube experiments, these models include a minimal set of reactions relevant to protein aggregation in a specific scenario. For instance, they are typically coarse-grained to the extent that they either entirely exclude intermediate species or consider a single oligomeric state (e.g., see refs. 3,32), due to the principle of model parsimony and limitations in data availability. Since we aimed at a unified description of aggregation in vitro, we propose a mathematical model that accounts for microscopic events physiologically related to uncontrolled aSyn accumulation in the literature, exploiting prior biological and mechanistic knowledge and a step-wise calibration on various test-tube aggregation datasets. A detailed comparison between our work and other models of aSyn aggregation, in terms of structure and parameter estimates, is available at Supplementary Table 1 and Supplementary Table 2.

The mathematical description of aggregation presented here incorporates competing nucleation reactions, suggesting a dominant role for secondary nucleation in aSyn aggregation and thus in anti-aSyn aggregation therapies. This result aligns with recent findings that highlight the role of this reaction in oligomer and fibril formation under physiological conditions, either with acidic[34,36] or neutral pH[35,39]. Parameters estimated at acidic pH successfully described fibril formation driven by secondary nucleation at neutral pH for medium-high seeding conditions. However, this result may rise some doubts given previous findings on pH-dependence of secondary nucleation. Specifically, Buell et al.[36] reported that secondary nucleation flux increases dramatically at acidic compared to neutral pH. However, the experimental setup required to reveal this pH dependence relied on very low seed levels (nM seeds vs. μM monomers). Therefore, our model suggests that seeding conditions can modulate the impact of pH on secondary nucleation-dependent processes. Yet, the specific mechanisms by which pH affects secondary nucleation rates require further investigation.

In line with previous work focused on stable oligomers[12,30,31], our model confirms the critical role of the kinetics of oligomer structural conversion in determining the overall fibril growth dynamics in the given aggregation scenarios. We considered two sequential oligomeric types connected by conformational changes with distinct rate constants, comparable to estimates of oligomer conversion rates from the literature[3,30–32]. The ratio $k_{c2}/k_{c1} = 0.15$ suggests that type-B oligomers predominate during aggregation, indicating higher stability than type-A oligomers. Given the higher toxicity of type-B oligomers, the conversion rate may be a crucial factor in controlling neuronal damage. Targeting this reaction may represent an effective approach adopted by intracellular defense mechanisms[3] and holds promise as a strategy for therapeutic intervention by molecular chaperones and small molecules. These results on oligomer conversion derive from model calibration using smFRET data and, thus, refer to long-lived oligomers. Given their prolonged presence and association with increased ROS production, long-lived oligomers represent a toxicologically relevant yet small fraction of the total oligomeric population. Indeed, recent methodologies indicate that short-lived oligomers are substantially more abundant. By investigating their kinetics under physiological neutral conditions (as described in ref. 35), our model confirmed previous results on short-lived oligomer formation driven by secondary nucleation and mainly balanced by oligomer dissociation, and suggests a higher stability of type-A compared to type-B species ($k_{c2}/k_{c1} \sim 2$). Such a kinetic dichotomy between transient and stable oligomeric species further points to fundamental differences in their biological roles. For instance, since their formation is catalyzed by fibrils, short-lived oligomers may act not only as bulk nucleation products influencing aggregation kinetics but also as sources of toxicity and aggregate spreading, through mechanisms that remains to be fully elucidated.

Xu et al.[35] modeled transient oligomers kinetics by integrating two processes: a complete nucleation-polymerization pathway - encompassing primary nucleation, fibril elongation, and secondary nucleation - and an oligomer formation/dissociation cycle catalyzed by fibrils. Focusing on the dominant mechanisms of oligomer formation and depletion, this approach suggests an off-pathway nature for short-lived oligomers while not excluding the presence of distinct on-pathway species. The model was calibrated in two steps: first to fibril mass data across seeding scenarios (1–10% seeds, Amylofit[35]) and then to oligomer data (0% and 1% seeds). Our work raises mechanistic questions about these oligomers. For example, do short-lived oligomers undergo structural conversion as their long-lived counterparts? Are both transient and stable oligomers on-pathway and governed by the same formation and depletion mechanisms? Our model assumes that both transient and stable oligomers are on-pathway to fibril formation and undergo sequential conformational changes (from type-A to type-B). Upon calibration on combined fibril and oligomer mass data, the model successfully reproduce fibril and oligomer profiles for various seeding conditions. This good performance, comparable to that in ref. 35, challenges the strictly off-pathway nature of microfluidic-detected oligomers. They could represent either early unstable intermediates or aggregation products generated alongside fibril formation. Nonetheless, their fibril-catalyzed formation makes them an integral part of the aggregation landscape. Further single molecule microfluidic data on transient species would be needed to address these mechanistic knowledge gaps. Overall, our quantitative analysis requires caution due to the sparsity and noisiness of these measurements compared to smFRET data. Expanding datasets obtained by minimally perturbative techniques, particularly time series under varying monomer concentrations, will be essential to better constrain model parameters and refine models that capture both short- and long-lived oligomers, thereby advancing our understanding of oligomer dynamics.

Building on previous mechanistic insights into aSyn-lipid interactions[16,32], we included aSyn monomer-lipid binding and vesicle-boosted fibril elongation in our model. These mechanisms capture the linear scaling of lipidic fibril concentration at plateau. However, the model does not fully account for the fibril growth phase in this aggregation scenario, suggesting hidden non-linear interactions between aSyn fibril and lipids. Future modeling efforts should explore this mechanism in collaboration with experimentalists. Additionally, further refinement should focus on the role of lipids in heterogeneous primary nucleation, a controversial aspect in lipidic aggregation research[15,16,32]. We assumed that heterogeneous primary nucleation occurs at air-water interfaces rather than on lipidic vesicles, as suggested by Dear et al.[16]. While lipid incorporation was modeled at the fibril elongation stage, we cannot exclude the possibility that some lipids integrate into intermediate species forming at the air-water interface during nucleation. A lipid monolayer at this interface could provide a ready supply of lipids, influencing the nucleation process. Since the concentration of heterogeneous nucleation sites is incorporated into the rate constant ($k_{max,I}$) in the model, any lipid-induced effect at this stage would be reflected in its value. Another refinement could involve monomer-vesicle binding. While our model assumes a fixed monomer count per vesicle, an alternative approach could account for vesicles with varying bound monomer counts, though this would require additional experimental data to characterize their distribution and impact on fibril elongation as well as on aSyn aggregation dynamics.

Exploring the interplay between pure and lipidic aggregation and the impact of lipid-to-aSyn ratio can offer insights into pathological mechanisms and can suggest potential therapeutic strategies. To this end, our model provides a virtual lab for investigating how the availability of free monomers and lipidic vesicles affects the dynamics of in vitro aSyn aggregation via pure and lipidic routes and how this may relate to PD onset and development. Integrating pure and lipidic aggregation preserved the qualitative behavior of lipidic fibrils across lipid-to-aSyn ratios: monomer excess inhibits lipidic fibril formation; vesicle surplus suppresses all aggregation by sequestering monomers; a balance between monomers and lipidic vesicles results in a

scaled yet non-linear increase of lipidic fibril mass and number concentrations with lost robustness of the plateau level of $\tilde{M}_{F,1}$ to variations in initial monomer concentration. As a result, total fibril mass concentration decreases monotonically with increasing lipid-to-aSyn ratios, reflecting the competitive interplay between the two pathways. Therefore, lipid and protein availability can reshape fibril composition and kinetics in this crosstalk, with relevant physiological and pathological implications. For example, the model can be used for testing different hypotheses on the in vitro formation and crowding of vesicular structures interspersed with aSyn filaments, hinting at the role of aSyn-lipid interactions in modulating Lewy body composition[13,14]. However, these insights, along with the Lewy body composition indexes introduced in this work, should be seen as indicative rather than directly informative of in vivo scenarios, given that the model does not account for aSyn production and degradation, as discussed below.

Given its confirmed crucial role in in vitro aSyn aggregation, the lipid-to-aSyn ratio could serve as a proxy for specific risk factors for Parkinson's disease, such as genetic alterations and aging. Specifically, investigating how variations of this control parameter affect aSyn dynamics can be relevant for understanding disease-associated mutations leading to aSyn overexpression, e.g., via gene duplication and triplication. Even small perturbations of free monomer concentrations can disrupt the physiological balance between free vesicles and monomeric aSyn and, thus, substantially affect aggregation. On the other hand, aging can be associated with lipid vesicle concentration alterations. As discussed in Kiechle et al.[40], age-related factors often lead to decreased local lipid-to-protein ratio. To showcase the model potential, we simulated an in silico scenario mimicking the conditions of a damaged dopaminergic neuron flooded with aSyn aggregates and the impact of oscillations in the DMPS to free aSyn monomer ratio (see Supplementary Note 6 and Supplementary Fig. 7). Our model suggests that such imbalances between available free vesicles and monomers can enhance aSyn aggregation. Overall, perturbations of the lipid-to-aSyn ratio may disrupt the balance between benign and harmful effects of aSyn-lipid interactions, leading to PD pathogenicity. Notably, the lipid-to-aSyn ratio can also serve as a proxy for the mechanism of action of candidate drugs targeting aSyn-lipid interactions or modulating vesicle concentrations, such as genipin. This iridoid glucoside is currently under investigation for its direct interaction with aSyn monomers, which alters the nucleation step, and its putative effect on lipid storage, which leads to reduced lipid-to-aSyn ratio[41]. Both modes of action and their impact on aSyn aggregation can be investigated through our model.

In these critical times, when clinical trials for PD continue to fail, modeling can play a crucial role in supporting the design of new therapeutic compounds and drugs currently under investigation in various ways. Besides affecting the local lipid concentration, a candidate compound can directly bind aSyn in one of its various states, e.g., monomers, oligomers, or fibrils, perturbing one or more mechanisms within the aggregation process. In this context, our model can facilitate the analysis of anti-aSyn aggregation compounds[42], such as those that have reached the clinical state of development, i.e., Anle-138b[43] and UCB-0599[44], other small molecules, e.g., EGCG and SynuClean-D, and nanobodies, e.g., NbSyn2 and NbSyn87[45]. Moreover, it can be used to investigate therapeutic strategies involving a combination of small molecules with different modes of action. As suggested by the results of the LSA analysis, it can also support the identification of potential pharmacological targets. In particular, our model suggests that inhibiting secondary nucleation may be an effective therapeutic strategy to reduce harmful oligomeric species, thus supporting the idea that developing compounds targeting fibril surfaces could be crucial for lowering aggregation inherent toxicity[16]. Indeed, fibrils are critical sites where oligomeric species form and lipids interact with growing fibrils, acting as a common element in both aggregation pathways. Such an effect is associated with various inhibitors of secondary nucleation, for example, small molecules binding the catalytic sites on fibril surfaces[46,47] and aminosterol compounds with high blood-brain barrier penetrability, e.g., trodusquemine[48,49]. Our model also predicts that inhibiting secondary nucleation can have a mixed impact on aSyn aggregation: while it reduces toxic type-B oligomers, its effect on fibril composition remains ambiguous. This intervention favors pure fibril formation but does not significantly reduce overall fibril mass concentration and lipidic fibril dominance. Given the uncertainty regarding whether lipidic or pure fibrils are more detrimental to neurons, the overall impact of this strategy remains unclear. Therefore, understanding the implications of lipidic dominance and clarifying the pathological roles of different fibril types is crucial to determining whether this intervention could effectively counteract aSyn aggregation.

When exploring mechanistic effects in test-tube experiments using chemical kinetics models[18], inherent challenges of translating results from in vitro to in vivo settings must be accounted. Indeed, there is a tight link between the contribution of each microscopic event to the overall aggregation and the solution conditions. For example, secondary nucleation has been proven to contribute to a different extent depending on the pH of the surrounding environment and seeding levels[34,36]. Moreover, in the presence of lipids, their identity strongly affects the aggregation kinetics[16,32], and DMPS SUVs have a different composition from vesicles found in a synaptic bouton or functional synaptosome[32]. On the other hand, we expect several aspects of aSyn aggregation highlighted by our model to translate into in vivo scenarios. Indeed, the monomer concentrations associated with the in vitro aggregation assays used for model calibration fall within the physiologically relevant range[50], given that aSyn reaches micromolar concentrations in synaptic boutons[51]. Moreover, as highlighted by recent studies[16,35,39], a wide range of lipids results in aSyn-lipid co-assemblies as the main species in the aggregation pathway, and secondary nucleation has a central role in aSyn aggregation also in neutral pH solutions under quiescent conditions. More generally, despite potential variations in rate constants and rate-limiting steps, the fundamental mechanisms of aSyn aggregation remain consistent. Therefore, although our model is calibrated for specific experimental conditions, it hinges on processes that retain in vivo translatability, such as oligomeric conversion, secondary nucleation, and fibril elongation via the incorporation of monomers and lipids. This consistency aligns with the holistic approach of QSP and PBPK frameworks, which integrate system-level dynamics to model complex biological processes.

To capture the impact of aSyn aggregation on neuronal function in vivo, future work should extend the model presented here to encompass additional mechanisms, particularly those involving fibril breakdown mechanisms. For example, based on its negligible impact on aggregation dynamics, we have chosen to disregard fibril depolymerization, i.e., the reverse of fibril elongation by monomer addition, as a contributing factor in our model. This process is significantly slower than other dominant aggregation events and becomes especially insignificant as monomer concentrations are depleted at equilibrium[31]. Moreover, our model does not include fibril disaggregation into oligomers. This modeling choice aligns with existing chemical kinetic models of aSyn aggregation, which typically exclude this reaction due to its negligible impact under standard experimental setups and its limited mechanistic role under physiological conditions[3,30,31,35]. Indeed, fibril disaggregation into oligomers has been observed primarily under destabilizing conditions, such as monomer-depleted environments or altered pH[3,52]. Moreover, this simplification supports the broader goal of integrating the model into a QSP framework, where excluding processes with minimal impact simplifies the model while still capturing the key features of aSyn aggregation relevant for drug development. Nevertheless, fibril disaggregation could play a more significant role in specific physiological contexts or under therapeutic interventions aimed at destabilizing fibrils. For example, fibril disaggregation can release cytotoxic oligomers that may accelerate neurodegeneration[3], and intracellular processes such as chaperone-mediated disaggregation could influence this pathway[53]. Future iterations of this model could incorporate fibril disaggregation to explore its potential contributions to disease progression and therapeutic outcomes, particularly in scenarios involving environmental or cellular stressors and enzymatic activity that promote fibril destabilization.

Current research highlights secondary nucleation as the candidate secondary mechanism governing aSyn aggregation, whereas fibril

fragmentation is typically excluded from models of test-tube fibril formation due to its minimal impact on early-time dynamics (hours or days). Indeed, under physiological conditions, experimental measurements suggest that fragmentation rates are low compared to secondary nucleation[35]. Nevertheless, this mechanism may become more relevant over longer timescales associated with disease progression (days to years), particularly in fibril length redistribution and potential prion-like spread. Fragmentation indeed generates shorter seeds (<50 nm) with enhanced cell penetration and high cytotoxicity[54], potentially accelerating neuropathological spread in later disease stages. Further extensions of this model could incorporate fragmentation delayed pathological role for multi-timescale simulations of Parkinson's disease progression. This would be particularly relevant in scenarios where monomer depletion approaches critical concentrations or where mechanical stresses become more pronounced (e.g., trauma, shear forces in CSF, or cellular motility). However, while fragmentation becomes the main reason for fibril number increase at full monomer depletion, in vivo systems rarely reach full depletion due to continuous protein production.

While total protein mass concentration remains constant in test-tube experiments, aggregation dynamics is regulated by monomer production and protein clearance in vivo. Therefore, another model extension would consist in adopting a modular and incremental strategy to integrate the standalone aggregation module with a minimal reaction set, accounting for protein synthesis, misfolding, and generic degradation mechanisms (e.g., Thompson et al.[55]). Such a model would provide insights into the interplay of aSyn aggregation and dysfunctional degradation and, thus, into PD pathogenesis. Indeed, while PD has commonly been identified as a proteinopathy, it is not merely a consequence of aSyn aggregation but manifests as a multifactorial disorder wherein various pathological mechanisms converge. Disrupted aSyn homeostasis, controlled by uncontrolled protein accumulation and age-related impairments of the degradation machinery, stands out among these processes. Therefore, targeting aSyn aggregation or degradation processes within the deregulated proteostasis network can be a promising strategy to slow down or halt PD progression. In this context, a mechanistic understanding of the role of aSyn aggregation in this intricate molecular landscape is critical for developing effective therapeutic interventions.

Although our model is rooted in in vitro findings, by offering a unified description of in vitro aggregation, it can serve both as a stand-alone tool for advancing therapeutic strategy design through molecular-level mechanistic insights and as a modular component in multiscale models.

Aligned with recent work in modeling neurodegenerative diseases[25,56,57], this model is well-suited for integration into a mechanistic framework that includes a brain compartment along with compartments representing aSyn detection sites, such as cerebrospinal fluid and blood. This approach would leverage data from ongoing clinical trials on various disease-modifying therapies[42,58,59]. More specifically, our work provides a ready-to-go model grounded in prior in vitro mechanistic knowledge that can be seamlessly integrated into larger modeling frameworks. Overall, within a QSP framework, our model might serve as a key building block for an intraneuronal model of disrupted aSyn homeostasis in Parkinson's disease.

Our work contributes to a coherent mechanistic understanding of aSyn aggregation by combining key findings and published in vitro data, acquired from various experimental conditions and through different techniques. The model corroborates mechanistic findings across diverse aggregation scenarios and provides insights into in vitro experimental outcomes. Therefore, it serves as a virtual lab for in silico experiments that, while impractical in vitro, may be relevant to in vivo biology, making it well-suited for integration into QSP and PBPK frameworks.

Material and methods

ODE system and deterministic implementation

The ODE system of the model of pure and lipidic aSyn aggregation consists of 12 variables, 12 reactions, and 18 parameters, listed in Table 1. Refer to Fig. 1 for a graphical representation of this model.

$$\frac{dm}{dt} = \underbrace{-nk_n m^n}_{\text{homogeneous primary nucl.}} \underbrace{-nk_{\max,I}\frac{m^n}{m^n+K_P^n}}_{\text{heterogeneous primary nucl.}} \underbrace{+nk_d A}_{\text{oligomer dissociation}} \underbrace{-nk_{\max,II}\frac{m^n}{m^n+K_S^n}\tilde{M}_{F,p}}_{\text{pure fibril secondary nucl.}} \underbrace{-nk_{\max,II}\frac{m^n}{m^n+K_S^n}\tilde{M}_{F,l}}_{\text{lipidic fibril secondary nucl.}}$$
$$\underbrace{-nk^*_{\max,II}\frac{m^n}{m^n+K_S^n}M_{F,*}}_{\text{newly generated fibril secondary nucl}} \cdot \underbrace{-k_{l1}mF_p}_{\text{pure fibril elongation}} \underbrace{-yk_{on}V_b\frac{k_{l2}mF_l}{k_{l2}m+yk_{on}V_b}}_{\text{vesicle-mediated (lipidic) fibril elongation}} \underbrace{+\frac{M_s}{\gamma}(-k^+mV_f+k^-V_b)}_{\text{monomer-vesicle binding}}$$

$$\frac{dA}{dt} = +k_n m^n + k_{\max,I}\frac{m^n}{m^n+K_P^n} - (k_d+k_{c1})A + k^p_{\max,II}\frac{m^n}{m^n+K_S^n}\tilde{M}_{F,p} + k^l_{\max,II}\frac{m^n}{m^n+K_S^n}\tilde{M}_{F,l} + k^*_{\max,II}\frac{m^n}{m^n+K_S^n}M_{F,*}$$

$$\frac{dB}{dt} = \underbrace{+k_{c1}A}_{\text{oligomer conversion}} \underbrace{-k_{c2}B}_{\text{fibril formation}}$$

$$\frac{dF^*}{dt} = +k_{c2}B \underbrace{-k_{l1}mF^*}_{F^* \text{ elongation}} \underbrace{-k_{on}V_bF^*}_{\text{vesicle}-F^* \text{ binding}}$$

$$\frac{dM_{F^*}}{dt} = +nk_{c2}B - k_{l1}mM_{F^*} - k_{on}V_bM_{F^*}$$

$$\frac{dF_p}{dt} = +k_{c2}B - k_{on}V_bF^*$$

$$\frac{dM_{F,p}}{dt} = +nk_{c2}B + k_{l1}mF_p - k_{on}V_bM_{F^*}$$

$$\frac{dF_l}{dt} = +k_{c2}B - k_{l1}mF^*$$

$$\frac{dM_{F,l}}{dt} = +nk_{c2}B - k_{l1}mM_{F^*} + yk_{on}V_b\frac{k_{l2}mF_l}{k_{l2}m+yk_{on}V_b}$$

$$\frac{dV_{F,b}}{dt} = +k_{on}V_b\frac{k_{l2}mF_l}{k_{l2}m+yk_{on}V_b}$$

$$\frac{dV_f}{dt} = -k^+mV_f + k^-V_b$$

$$\frac{dV_b}{dt} = k^+mV_f - k^-V_b - k_{on}V_b\frac{k_{l2}mF_l}{k_{l2}m+yk_{on}V_b}$$

$$m_{TOT} = m + m_b + m_{F,b} + n(A+B) + M_{F,TOT} \quad \textbf{(monomer conservation law)}$$

$$V_{TOT} = V_f + V_b + V_{F,b} \quad \textbf{(vesicle conservation law)}$$

where $\tilde{M}_{F,\mathrm{p}} = M_{F,\mathrm{p}} - M_{F,*}$, $\tilde{M}_{F,\mathrm{l}} = M_{F,\mathrm{l}} - M_{F,*}$, and $M_{F,\mathrm{TOT}} = M_{F,\mathrm{p}} + M_{F,\mathrm{l}} - M_{F^*} = \tilde{M}_{F,\mathrm{p}} + \tilde{M}_{F,\mathrm{l}} + M_{F,*}$. Also, $m_{\mathrm{b}} = \frac{M_s}{y} V_{\mathrm{b}}$ and $m_{F,\mathrm{b}} = \frac{M_s}{\gamma} V_{F,\mathrm{b}}$. Given an initial lipid amount $\mathrm{DMPS}_{\mathrm{TOT}}$, the total vesicle concentration $V_{\mathrm{TOT}} = \mathrm{DMPS}_{\mathrm{TOT}}/M_s$. Type-A and type-B oligomer mass concentrations correspond to $M_A = nA$ and $M_B = nB$, respectively.

We implemented the ODE system in MATLAB 2024a, using the built-in ODE solver function ode23s for simulations.

Master equation approach

Within the modeling framework proposed by Knowles and colleagues[17,33], the deterministic model proposed here results from a moment-based approximation of a master equation, relying on the chemical kinetic representation of protein aggregation[17]. The master equation approach describes in probabilistic terms the time course of the species involved in the system and identified by their monomer count. Specifically, this stochastic representation presents the evolution of the molecule number of filaments of length j at time t, i.e., $f(j,t)$, using the concentration of monomers at time t. The resulting master equation summarizes an infinite system of non-linear differential equations. By extracting the zero-th and first moments, e.g., $F_{\mathrm{X}}(t) = \sum_{j>n} f(j,t)$ and $M_{F,\mathrm{X}} = \sum_{j>n} jf(j,t)$, we obtain the corresponding ODE deterministic system describing the dynamics of aggregate number and mass concentrations, respectively.

Note that the reaction flow of lipid-mediated fibril elongation has been taken from Dear et al.[16]. This term relies on the assumption that newly generated fibrils F^* and fibrils with vesicles bound y monomers away from the fibril ends $F_{\mathrm{l},y}$ can bind a new monomer-coated vesicle, whereas the other fibrillar species $F_{\mathrm{l},i}$ $(0 \le i < y)$ can only elongate with rate constant k_{l2}. By adopting a mean field approach as in[16], we derived the differential equations:

$$\frac{dF^*}{dt} = k_{\mathrm{n}} m^n + k_{\max,\mathrm{I}} \frac{m^n}{m^n + K_p^n} + k_{\max,\mathrm{II}} \frac{m^n}{m^n + K_s^n} M_{F,\mathrm{l}} - k_{\mathrm{on}} V_{\mathrm{b}} (F^* + F_{\mathrm{l},y})$$
$$\frac{dF_{\mathrm{l},0}}{dt} = k_{\mathrm{on}} V_{\mathrm{b}} (F_{\mathrm{l},y} + F^*) - k_{\mathrm{l2}} m F_{\mathrm{l},0}$$
$$\frac{dF_{\mathrm{l},i}}{dt} = k_{\mathrm{l2}} m F_{\mathrm{l},i-1} - k_{\mathrm{l2}} m F_{\mathrm{l},i}$$
$$\frac{dF_{\mathrm{l},y}}{dt} = k_{\mathrm{on}} V_{\mathrm{b}} (F_{\mathrm{l},y} + F^*) - k_{\mathrm{l2}} m F_{\mathrm{l},0}$$

Assuming that the nucleation rates are negligible compared to the elongation rates and approximating to a pre-equilibrium between the different species[16] result into

$$F_{\mathrm{l},0} = \frac{k_{\mathrm{on}} V_{\mathrm{b}}}{k_{\mathrm{l2}} m} (F_{\mathrm{l},y} + F^*)$$
$$F_{\mathrm{l},i} = F_{\mathrm{l},i-1} \qquad (0 < i < y)$$
$$F^* + F_{\mathrm{l},y} = \frac{k_{\mathrm{l2}} m}{k_{\mathrm{on}} V_{\mathrm{b}}} F_{\mathrm{l},y-1}$$
$$F_{\mathrm{l}} = \sum_{i=0}^{y} F_{\mathrm{l},i} + F^* = y F_{\mathrm{l},0} + F^* = \left(1 + y \frac{k_{\mathrm{on}} V_{\mathrm{b}}}{k_{\mathrm{l2}} m}\right)(F_{\mathrm{l},y} + F^*)$$

leading to the lipid-mediated elongation term

$$\frac{dM_{F,\mathrm{l}}}{dt} = \sum_{i=0}^{y-1} k_{\mathrm{l2}} m F_{\mathrm{l},i} + \varepsilon = y k_{\mathrm{l2}} m F_{\mathrm{l},0} + \varepsilon = \frac{k_{\mathrm{on}} V_{\mathrm{b}}}{k_{\mathrm{l2}} m} (F_{\mathrm{l},y} + F^*) + \varepsilon$$
$$= y \frac{k_{\mathrm{on}} V_{\mathrm{b}} k_{\mathrm{l2}} m F_{\mathrm{l}}}{y k_{\mathrm{on}} V_{\mathrm{b}} + k_{\mathrm{l2}} m} + \varepsilon$$

where ε represents the additional terms governing $M_{F,\mathrm{l}}$ time derivative.

Model calibration and validation

Calibration of pure protein aggregation. Given the crucial role of oligomers in the aggregation pathway, we first focused on available data of aSyn oligomerization in solution, corresponding to the first pure protein aggregation scenario[30]. Retrieving time-series data on oligomer levels proves challenging due to their diverse and transient nature; smFRET stands out among the few experimental techniques that can monitor oligomers' time evolution (e.g., quantitative size exclusion chromatography, multispectral microchip free-flow electrophoresis) as it can differentiate between type-A and type-B oligomers linked to low and high FRET levels. Therefore, we used the available smFRET measurements of monomers and oligomers to calibrate oligomeric conversion and fibril formation, in addition to primary nucleation reactions. Conversely, rate constants associated with oligomer dissociation and fibril elongation were set to fixed values derived from the literature[31,36]. Drawing on existing biological insights into the role of secondary events in this scenario, we switched off secondary nucleation and ruled out fibril fragmentation in our model. Indeed, fibril-catalyzed nucleation plays a marginal role compared to homogeneous and heterogeneous primary nucleation, especially at early reaction times, when high fibril levels are not reached yet. Moreover, even though constant agitation is known to promote fibril fragmentation, we excluded this reaction from the model diagram upon assessment of its negligible impact on early-time dynamics. At the same time, constant agitation promotes heterogeneous primary nucleation by introducing shearing forces or increasing turnover at the air-water interface[34,60]. Therefore, while mechanical stress is not explicitly modeled, its effects are implicitly captured through the calibrated parameters, particularly by the heterogeneous nucleation rate constant.

Approaching a more physiologically relevant scenario as compared to shaking-induced aggregation, we calibrated the model to reproduce the dynamics of pure aSyn aggregation triggered with preformed fibril seeds and exacerbated by a pH shift from neutral to mildly acidic. Secondary nucleation plays a predominant role in this setting compared to primary nucleation[34]. Parameters associated with this mechanism were fitted while keeping those related to primary nucleation mechanisms fixed, by leveraging the results from the initial calibration step. Note that we estimated the rate constant of secondary nucleation on pure and newly generated fibrils as a single parameter $k_{\max,\mathrm{II}}$ (i.e., $k^{\mathrm{p}}_{\max,\mathrm{II}} = k^{*}_{\max,\mathrm{II}}$). Simultaneously, we adjusted the rate constants governing oligomer conformational changes, maintaining a fixed ratio k_{c2}/k_{c1}. In contrast to the first calibration step, the model was calibrated on measurements of fibril mass concentration by Thioflavin-T (ThT) dye fluorescence. Although more precise than smFRET, this standard technique cannot provide oligomer data but only detect fibril levels.

In addition to smFRET, single-molecule microfluidics can also detect oligomer mass data[35]. Here, we focused on ThT-derived fibril mass and single molecule FFE-derived oligomer mass data obtained under solution conditions that mimic the cytosolic environment (neutral pH and physiological ionic strength). To recalibrate the model for 0% and 1% seeded aggregation, we (i) retained primary nucleation and fibril elongation estimates from the second calibration scenario, (ii) increased the oligomer dissociation rate constant ($k_{\mathrm{d}} = 1\ \mathrm{h}^{-1}$ vs. $k_{\mathrm{d}} = 2.4 \times 10^{-3}\ \mathrm{h}^{-1}$ in previous calibrations), (iii) removed constraints on oligomeric conversion rate constants for long-lived oligomeric species (i.e., $k_{c2} = 0.15 k_{c1}$). As for the previous scenario, we estimated the rate constant of secondary nucleation on pure and newly generated fibrils as a single parameter $k_{\max,\mathrm{II}}$ (i.e., $k^{\mathrm{p}}_{\max,\mathrm{II}} = k^{*}_{\max,\mathrm{II}}$).

Calibration of lipid-mediated aggregation. We considered another biologically meaningful scenario related to aSyn normal functions in the synapses. DMPS vesicles are introduced in neutral pH solutions with monomers at different lipid-to-aSyn ratios, obtained by adjusting the initial lipid amount while maintaining a constant total monomer concentration. DMPS phospholipids, commonly used in lipid-mixing vesicle preparation to form thin membranes, promote significant lipid uptake in aSyn co-aggregates[14]. This in vitro aggregation assay has proven valuable for analyzing lipidic aSyn aggregation. By leveraging this experimental setup, Dear et al.[16] challenged the traditional perspective that lipid bilayers act as catalysts for primary nucleation, increasing the local protein concentration on their surface to facilitate aggregation[32]. While lipids may have a role in primary nucleation, their primary function is

actively boosting fibril elongation, which governs the aggregation process[15,16]. We integrated these recent mechanistic findings into the model structure and set some of the parameters associated with lipidic interactions (K_D = 3.8e-01 μM, $\gamma \sim 30$, $M_s = 6000$, and $7.5 \le k_{on}/k_{l2} \le 16$) to values provided by the existing literature[16,32].

We relaxed the pre-equilibrium assumption on monomer-vesicle binding set by Dear et al.[16]. As a result, model calibration required assessing the rate constant of monomer-vesicle unbinding k_-, such that $K_D = k_-/k_+$, and fitting the coefficient of vesicle-mediated fibril elongation γ as a free parameter instead of deriving it directly from stoichiometric relationships. To obtain this parameter value, Dear et al.[16] used the formula $\gamma = M_s/\gamma - M_s/\chi$, where the stoichiometry of lipid-to-protein in lipidic fibrils χ was experimentally estimated at ~15 lipids per protein monomer under optimal conditions[16,32]. Without pre-equilibrium, the assumption of a fixed stoichiometry no longer strictly applies, and the explicit relationship between γ, χ, and other parameters becomes dynamic/less deterministic, with deviations in stoichiometry arising under sub-optimal conditions. In our model, γ represents no longer a fixed number but an empirical average number of monomers added per vesicle binding event; thus, it reflects an average behavior influenced by experimental conditions such as lipid-to-protein ratio, vesicle size (M_s), and binding kinetics (k_+ and k_-). The estimated value still aligns with the values obtained in the literature. Nevertheless, treating γ as a fitted parameter can provide flexibility in modeling variability across experimental conditions while capturing essential features of lipid-mediated co-elongation and maintaining consistency with experimental observations.

Furthermore, we assumed that lipidic fibrils elongate at the same rate constant as pure fibrils, i.e., $k_{l1} = k_{l2}$, with the parameter value derived from the literature[36].

Based on parameter estimates from prior calibrations, we adjusted the rate constants related to oligomer structural conversions while keeping their ratio fixed. Moreover, we switched off all nucleation reactions except for heterogeneous primary nucleation (estimated), which has been identified as the predominant nucleation reaction in this experimental setting[16]. In line with this, the fitting procedure suggested a negligible impact of secondary nucleation in this experimental scenario ($k^{l}_{max,II} = k^{*}_{max,II} = 0$).

Optimization algorithm and uncertainty quantification. The parameter estimation procedure relied on a global stochastic optimization method computing the covariance matrix of the search distribution to estimate unknown model parameters, namely, the covariance-based evolutionary optimization (CMA-ES) algorithm[61]. The optimization problem corresponded to minimizing a weighted least squares objective function tailored for each calibration scenario. To avoid model overfitting and take into account the differences in initial monomer and lipid concentrations, we calibrated the aggregation module on multiple time-series for the considered species in the system corresponding to the highest and lowest initial monomer concentrations/lipid-to-monomer ratios. Complementarily, we validated the model on the time series related to intermediate levels of initial monomer concentrations and lipid-to-monomer ratios.

To perform uncertainty quantification, we randomly sampled 1000 parameter sets from a standard normal distribution centered in the parameter estimates with coefficient of variation of 20% (10% for γ). We then run model simulations for each parameter set and computed the median and the 5th and 95th percentiles of the time series distribution for each model species.

Aggregation metrics

For comparison across in silico experiments, we computed different metrics that directly relate to aggregation:

- the oligomer peak level and time.
- the final level of pure, lipidic, and newly generated fibril mass concentration normalized to the total monomer concentration (i.e., $\tilde{M}_{F,p}$, $\tilde{M}_{F,l}$, and $M_{F,*}$ relative abundance), along with the corresponding half-time.
- the final level of pure, lipidic, and newly generated fibril number concentration normalized to the total fibril concentration (i.e., $\tilde{F}_p$, $\tilde{F}_l$, and F^* relative abundance), serving as a measure of the composition of the fibrillar population.
- the propensity of newly generated fibrils to undergo lipidic over pure protein aggregation normalized for the time range, identified by

$$\int_0^{t_f} \frac{k_{on} V_b(t)}{k_{l1} m(t) + k_{on} V_b(t)} dt,$$

  serving as a measure of the relative occurrence of the two reactions and, thus, determining the overall dominance of lipidic fibril formation over pure protein fibril formation.
- Lewy body composition indexes measuring the composition of Lewy body-like structures that result from our in vitro model system. These inclusions are not direct analogs of the cytoplasmic Lewy bodies in PD patients. Instead, they emerge as a natural outcome of in vitro aggregation, where "LB" seeds form through fibril-fibril interactions, and growth occurs through further fibril incorporation. The indexes introduced below track contributions of different fibril types. Given AUC(·) as the area under the curve over a specified time interval (i.e., $\mathrm{AUC}(x(t)) = \int_0^T x(t)\,dt$), we define:
  – self-contribution indexes for pure, lipidic, and newly generated fibrils:

$$I^{p} = \frac{\mathrm{AUC}(\tilde{F}_p^2)}{\mathrm{AUC}(\tilde{F}_{TOT}^2)} \qquad I^{l} = \frac{\mathrm{AUC}(\tilde{F}_l^2)}{\mathrm{AUC}(\tilde{F}_{TOT}^2)} \qquad I^{*} = \frac{\mathrm{AUC}(\tilde{F}_*^2)}{\mathrm{AUC}(\tilde{F}_{TOT}^2)} \tag{5}$$

  which sum to $I^{self} = I^{p} + I^{l} + I^{*} = \frac{\sum_{i\in\{p,l,*\}} \mathrm{AUC}(\tilde{F}_i^2)}{\mathrm{AUC}(\tilde{F}_{TOT}^2)}$.

  – a cross-contribution index for interactions between different fibril types:

$$I^{cross} = \frac{2\sum_{i,j\in\{p,l,*\}} \mathrm{AUC}(\tilde{F}_i \tilde{F}_j)}{\mathrm{AUC}(\tilde{F}_{TOT}^2)} \tag{6}$$

  By definition, $I^{self} + I^{cross} = 1$, ensuring a complete decomposition. A detailed derivation of these indexes is provided in Supplementary Note 5.

Local sensitivity analysis

We carried out a local sensitivity analysis (LSA) to quantify the impact of the model parameters on the system dynamics. For each parameter in $\mathbf{p} = (p_1, \ldots, p_j, \ldots, p_m)$, we computed a logarithmic sensitivity index (SI) based on the area-under-the-curve (AUC) of each model variables in $\mathbf{x} = (x_1, \ldots, x_i, \ldots, x_n)$ within the experimental time interval $[0, t_f]$. Relying on a numerical approximation given by the second order central finite difference formula, the sensitivity index $S_{i,j}$ associated with the model variable x_i and the $\delta = \pm 1\%$ perturbation of the parameter p_j from its nominal value was obtained as

$$\begin{aligned} SI_{i,j} &= \frac{\partial \log \mathrm{AUC}(x_i(p_j))}{\partial \log p_j} = \frac{\partial \mathrm{AUC}(x_i(p_j))}{\partial p_j} \frac{p_j}{x_i(p_j)} \\ &= \frac{\mathrm{AUC}(x_i(p_j + \delta p_j)) - \mathrm{AUC}(x_i(p_j - \delta p_j))}{2\delta p_j} \frac{p_j}{\mathrm{AUC}(x_i(p_j))} \end{aligned}$$

where $\mathrm{AUC}(x_i(p_j)) = \int_0^{t_f} x_i(p_j, t)dt$, with $x_i(p_j, t)$ denoting the i-th model variable at time t considering the nominal value of the j-th parameter p_j.

Data availability

This study did not generate any new experimental data. All datasets used in this research were obtained from published literature, with appropriate citations provided. The mathematical model results are provided in the Supplementary Data File.

Code availability

The model code and parameters are available at https://github.com/cosbi-research/aSynAggMod. Additionally, the provided code enables the reproduction of Figure 4 from the manuscript.

Received: 23 September 2024; Accepted: 13 May 2025;
Published online: 14 June 2025

References

1. Simuni, T. et al. A biological definition of neuronal α-synuclein disease: towards an integrated staging system for research. *Lancet Neurol.* **23**, 178–190 (2024).
2. Soto, C. et al. Toward a biological definition of neuronal and glial synucleinopathies. *Nat. Med.* **31**, 396–408 (2025).
3. Cremades, N. et al. Direct observation of the interconversion of normal and toxic forms of α-synuclein. *Cell* **149**, 1048–1059 (2012).
4. Zunke, F. et al. Reversible conformational conversion of α-synuclein into toxic assemblies by glucosylceramide. *Neuron* **97**, 92–107 (2018).
5. Gracia, P., Camino, J. D., Volpicelli-Daley, L. & Cremades, N. Multiplicity of α-synuclein aggregated species and their possible roles in disease. *Int. J. Mol. Sci.* **21**, 8043 (2020).
6. Cascella, R. et al. The release of toxic oligomers from α-synuclein fibrils induces dysfunction in neuronal cells. *Nat. Commun.* **12**, 1814 (2021).
7. Fusco, G. et al. Structural basis of membrane disruption and cellular toxicity by α-synuclein oligomers. *Science* **358**, 1440–1443 (2017).
8. Alam, P., Bousset, L., Melki, R. & Otzen, D. E. α-synuclein oligomers and fibrils: a spectrum of species, a spectrum of toxicities. *J. Neurochem.* **150**, 522–534 (2019).
9. Paslawski, W., Mysling, S., Thomsen, K., Jørgensen, T. J. & Otzen, D. E. Co-existence of two different α-synuclein oligomers with different core structures determined by hydrogen/deuterium exchange mass spectrometry. *Angewandte Chem.* **126**, 7690–7693 (2014).
10. Lorenzen, N. et al. The role of stable α-synuclein oligomers in the molecular events underlying amyloid formation. *J. Am. Chem. Soc.* **136**, 3859–3868 (2014).
11. Cremades, N., Chen, S. & Dobson, C. Structural characteristics of α-synuclein oligomers. *Int. Rev. Cell Mol. Biol.* (Academic Press, 2017).
12. Dear, A. J. et al. Identification of on- and off-pathway oligomers in amyloid fibril formation. *Chem. Sci.* **11**, 6236–6247 (2020).
13. Shahmoradian, S. H. et al. Lewy pathology in Parkinson's disease consists of crowded organelles and lipid membranes. *Nat. Neurosci.* **22**, 1099–1109 (2019).
14. Hellstrand, E., Nowacka, A., Topgaard, D., Linse, S. & Sparr, E. Membrane lipid co-aggregation with α-synuclein fibrils. *PloS ONE* **8**, e77235 (2013).
15. Galvagnion, C. et al. Structural characterisation of α-synuclein–membrane interactions and the resulting aggregation using small angle scattering. *Phys. Chem. Chem. Phys.* **26**, 10998–11013 (2024).
16. Dear, A. J. et al. Molecular mechanism of α-synuclein aggregation on lipid membranes revealed. *Chem. Sci.* **15**, 7229–7242 (2024).
17. Knowles, T. P. et al. An analytical solution to the kinetics of breakable filament assembly. *Science* **326**, 1533–7 (2009).
18. Meisl, G., Knowles, T. P. & Klenerman, D. Mechanistic models of protein aggregation across length-scales and time-scales: From the test tube to neurodegenerative disease. *Front. Neurosci.* **16**, 909861 (2022).
19. Meisl, G. et al. Molecular mechanisms of protein aggregation from global fitting of kinetic models. *Nat. Protoc.* **11**, 252–272 (2016).
20. Rinauro, D. J., Chiti, F., Vendruscolo, M. & Limbocker, R. Misfolded protein oligomers: mechanisms of formation, cytotoxic effects, and pharmacological approaches against protein misfolding diseases. *Mol. Neurodegen.* **19**, 1–32 (2024).
21. Hallacli, E. et al. The parkinson's disease protein alpha-synuclein is a modulator of processing bodies and mrna stability. *Cell* **185**, 2035–2056 (2022).
22. Sharma, M. & Burré, J. α-synuclein in synaptic function and dysfunction. *Trends Neurosci.* **46**, 153–166 (2023).
23. Killinger, B. A., Melki, R., Brundin, P. & Kordower, J. H. Endogenous alpha-synuclein monomers, oligomers and resulting pathology: let's talk about the lipids in the room. *npj Parkinson's Dis.* **5**, 23 (2019).
24. Righetti, E., Antonello, A., Marchetti, L., Domenici, E. & Reali, F. Mechanistic models of α-synuclein homeostasis for parkinson's disease: A blueprint for therapeutic intervention. *Front. Appl. Mathe. Stat.* **8**, 1060489 (2022).
25. Geerts, H. et al. A combined pbpk and qsp model for modeling amyloid aggregation in alzheimer's disease. *CPT: Pharmacometrics Syst. Pharmacol.* **12**, 444–461 (2023).
26. Bloomingdale, P. et al. Hallmarks of neurodegenerative disease: A systems pharmacology perspective. *CPT: Pharmacometrics Syst. Pharmacol.* **11**, 1399–1429 (2022).
27. Cassotta, M. et al. The future of Parkinson's disease research: a new paradigm of human-specific investigation is necessary… and possible. *ALTEX - Alternatives to animal experimentation* **2022**, 694–709 (2022).
28. Menon, G., Bakshi, S. & Krishnan, J. The interaction of core modules as a basis for elucidating network behavior determining parkinson's disease pathogenesis. *CPT: Pharmacometrics Syst. Pharmacol.* **13**, 335 (2024).
29. Denaro, C., Stephenson, D., Müller, M. L., Piccoli, B. & Azer, K. Advancing precision medicine therapeutics for parkinson's utilizing a shared quantitative systems pharmacology model and framework. *Front. Syst. Biol.* **4**, 1351555 (2024).
30. Iljina, M. et al. Kinetic model of the aggregation of α-synuclein provides insights into prion-like spreading. *Proc. Natl. Acad. Sci. USA* **113**, E1206–E1215 (2016).
31. Dear, A. J. et al. Kinetic diversity of amyloid oligomers. *Proc. Natl. Acad. Sci. USA* **117**, 12087–1294 (2020).
32. Galvagnion, C. et al. Lipid vesicles trigger α-synuclein aggregation by stimulating primary nucleation. *Nat. Chem. Biol.* **11**, 229–234 (2015).
33. Oosawa, F. & Kasai, M. A theory of linear and helical aggregations of macromolecules. *J. Mol. Biol.* **4**, 10–21 (1962).
34. Gaspar, R. et al. Secondary nucleation of monomers on fibril surface dominates α-synuclein aggregation and provides autocatalytic amyloid amplification. *Q. Rev. Biophys.* **50**, e6 (2017).
35. Xu, C. K. et al. α-synuclein oligomers form by secondary nucleation. *Nat. Commun.* **15**, 7083 (2024).
36. Buell, A. K. et al. Solution conditions determine the relative importance of nucleation and growth processes in α-synuclein aggregation. *Proc. Natl. Acad. Sci.* **111**, 7671–7676 (2014).
37. Froula, J. M. et al. Defining α-synuclein species responsible for Parkinson's disease phenotypes in mice. *J. Biol. Chem.* **294**, 10392–10406 (2019).
38. Hijaz, B. A. & Volpicelli-Daley, L. A. Initiation and propagation of α-synuclein aggregation in the nervous system. *Mol. Neurodegen.* **15**, 1–12 (2020).
39. Horne, R. I. et al. Secondary processes dominate the quiescent, spontaneous aggregation of α-synuclein at physiological ph with sodium salts. *ACS Chem. Neurosci.* **14**, 3125–3131 (2023).
40. Kiechle, M., Grozdanov, V. & Danzer, K. M. The role of lipids in the initiation of α-synuclein misfolding. *Front. Cell Dev. Biol.* **8**, 562241 (2020).
41. Rosado-Ramos, R. et al. Genipin prevents alpha-synuclein aggregation and toxicity by affecting endocytosis, metabolism and lipid storage. *Nat. Commun.* **14**, 1918 (2023).
42. Fields, C. R., Bengoa-Vergniory, N. & Wade-Martins, R. Targeting alpha-synuclein as a therapy for Parkinson's disease. *Front. Mol. Neurosci.* **12**, 299 (2019).

43. Antonschmidt, L. et al. The clinical drug candidate anle138b binds in a cavity of lipidic α-synuclein fibrils. *Nat. Commun.* **13**, 5385 (2022).
44. Schwarz, T. C. et al. High-resolution structural information of membrane-bound α-synuclein provides insight into the moa of the anti-parkinson drug ucb0599. *Proc. Natl. Acad. Sci. USA* **120**, e2201910120 (2023).
45. Iljina, M. et al. Nanobodies raised against monomeric α-synuclein inhibit fibril formation and destabilize toxic oligomeric species. *BMC Biol.* **15**, 1–14 (2017).
46. Staats, R. et al. Screening of small molecules using the inhibition of oligomer formation in α-synuclein aggregation as a selection parameter. *Commun. Chem.* **3**, 191 (2020).
47. Horne, R. I. et al. Discovery of potent inhibitors of α-synuclein aggregation using structure-based iterative learning. *Nat. Chem. Biol.* **20**, 634–645 (2024).
48. Perni, M. et al. Multistep inhibition of α-synuclein aggregation and toxicity *in* vitro and *in* vivo by trodusquemine. *ACS Chem. Biol.* **13**, 2308–2319 (2018).
49. Limbocker, R. et al. Trodusquemine displaces protein misfolded oligomers from cell membranes and abrogates their cytotoxicity through a generic mechanism. *Commun. Biol.* **3**, 435 (2020).
50. Rabe, M. et al. On-surface aggregation of α-synuclein at nanomolar concentrations results in two distinct growth mechanisms. *ACS Chem. Neurosci.* **4**, 408–417 (2013).
51. Wilhelm, B. G. et al. Composition of isolated synaptic boutons reveals the amounts of vesicle trafficking proteins. *Science* **344**, 1023–1028 (2014).
52. Picotti, P. et al. Amyloid fibril formation and disaggregation of fragment 1-29 of apomyoglobin: insights into the effect of ph on protein fibrillogenesis. *J. Mol. Biol.* **367**, 1237–1245 (2007).
53. Bigi, A., Cascella, R., Chiti, F. & Cecchi, C. Amyloid fibrils act as a reservoir of soluble oligomers, the main culprits in protein deposition diseases. *Bioessays* **44**, 2200086 (2022).
54. Xue, W.-F. et al. Fibril fragmentation enhances amyloid cytotoxicity. *J. Biol. Chem.* **284**, 34272–34282 (2009).
55. Thompson, T. B., Meisl, G., Knowles, T. P. & Goriely, A. The role of clearance mechanisms in the kinetics of pathological protein aggregation involved in neurodegenerative diseases. *J. Chem. Phys.* **154**, 125101 (2021).
56. Ramakrishnan, V. et al. Quantitative systems pharmacology model of the amyloid pathway in alzheimer's disease: Insights into the therapeutic mechanisms of clinical candidates. *CPT: Pharmacometrics Syst. Pharmacol.* **12**, 62–73 (2023).
57. Geerts, H., Bergeler, S., Walker, M., Van der Graaf, P. H. & Courade, J.-P. Analysis of clinical failure of anti-tau and anti-synuclein antibodies in neurodegeneration using a quantitative systems pharmacology model. *Sci. Rep.* **13**, 14342 (2023).
58. Pagano, G. et al. Trial of prasinezumab in early-stage parkinson's disease. *N. Engl. J. Med.* **387**, 421–432 (2022).
59. Lang, A. E. et al. Trial of cinpanemab in early parkinson's disease. *N. Engl. J. Med.* **387**, 408–420 (2022).
60. Campioni, S. et al. The presence of an air–water interface affects formation and elongation of α-synuclein fibrils. *J. Am. Chem. Soc.* **136**, 2866–2875 (2014).
61. Reali, F., Priami, C. & Marchetti, L. Optimization algorithms for computational systems biology. *Front. Appl. Mathe. Stat.* **3**, 6 (2017).

Acknowledgements

The authors would like to thank Prof. Giovanni Piccoli, Prof. Andrea Pugliese, Dr. Alessio Paris, Dr. Mattia Volta, and Stefano Giampiccolo for their insightful suggestions, comments, and collaborative efforts in preparing this manuscript. FR is member of the Gruppo Nazionale Calcolo Scientifico-Istituto Nazionale di Alta Matematica (GNCS-INdAM).

Author contributions

E.R. and F.R. designed and wrote the manuscript. E.D. supervised the work and discussed the results. L.M. provided feedback on the manuscript. All authors edited and reviewed the manuscript.

Competing interests

The authors declare no competing interests.

Additional information

Supplementary information The online version contains supplementary material available at https://doi.org/10.1038/s42004-025-01558-3.

Correspondence and requests for materials should be addressed to Elena Righetti or Federico Reali.

Peer review information *Communications Chemistry* thanks Harshbir Singh Sandhu and the other, anonymous, reviewers for their contribution to the peer review of this work. Peer reviewer reports are available.